Materials Advances

ROYAL SOCIETY OF CHEMISTRY

PAPER

View Article Online
View Journal | View Issue

Check for updates

Cite this: *Mater. Adv.*, 2025, **6**, 7552

Engineering of two-in-one Fe@Eu nanoparticles through hydrothermal synthesis: bimetallic hybrids for theranostic applications

Evangelia Tsitsou,[a] Danai Prokopiou,[a] Athina Papadopoulou,[a] Alexandros K. Bikogiannakis,[b] Georgios Kyriakou,[b] Elias Sakellis,[cd] Nikos Boukos,[c] Marios Kostakis,[e] Nikolaos S. Thomaidis[e] and Eleni K. Efthimiadou*[a]

Received 20th June 2025,
Accepted 25th August 2025

DOI: 10.1039/d5ma00659g

rsc.li/materials-advances

This study focuses on the synthesis of bimetallic Fe@Eu hybrid nanoparticles (NPs), combining structural and morphological characterization with an *in vitro* biological evaluation. By merging the superparamagnetic behavior of iron oxide nanoparticles (IONPs) with the distinctive optical properties of europium, these hybrid NPs emerge as strong candidates for a range of biomedical applications, particularly in cancer imaging and therapy. Magnetic IONPs were synthesized *via* co-precipitation and surface-modified with citrate to enhance colloidal stability. Europium was then introduced at varying Fe : Eu molar ratios (1 : 3, 1 : 1, and 1 : 0.25). Structural and morphological characterization confirmed the successful fabrication of the hybrids. DLS analysis demonstrated the excellent colloidal stability required for biomedical deployment. FT-IR, pXRD, and XPS verified the formation of magnetite and the successful incorporation of europium, which appeared as europium hydroxide nanorods. TEM elemental mapping further confirmed the co-existence of iron and europium within the same nanostructures. PL measurements revealed dual fluorescence capabilities, corroborated by widefield optical fluorescence microscopy, reinforcing their potential in multimodal imaging. *In vitro* studies showed efficient cellular internalization with minimal cytotoxicity. Mechanistic insights pointed to mild cell cycle disruption, moderate ROS generation, and apoptosis induction as part of the NPs' biological activity.

Introduction

Metal-based nanomaterials have gained particular interest in recent years, as they possess chemical and optical properties that make them ideal for use in a variety of applications,[1] such as photonics, sensors, catalysis, and biomedicine.[2] Divalent and trivalent metal ions from almost all metal salts are used as starting materials, which are reduced to the desired metallic nanoparticles (NPs) with appropriate reducing agents.[3] Among different metallic ions, iron emerges as an element of major importance due to its biocompatibility and essential role in biological systems, making it highly advantageous for the development of functional NPs.[4,5] At the nanoscale, iron is used in its oxide forms. These iron oxide nanoparticles (IONPs) exhibit the so-called "quantum size effect", whereby their optical, magnetic, and electrical properties are influenced by interactions at the level of individual atoms or molecules, rather than by bulk-averaged quantum effects.[6,7]

Surface modification on IONPs is carried out using various organic, inorganic or polymeric materials activating numerous properties and leading to a plethora of applications. Incorporation of bioactive molecules, such as nucleotides, proteins, antibodies, and drugs, makes IONPs particularly useful in the biomedical field.[7,8] Magnetic NPs have been studied for biomedical applications since the 1990s, while IONPs have already been approved by the Food and Drug Administration (FDA) for use in medicine and food.[9] Regardless of the type of application, IONPs possess properties that enhance their effectiveness, such as superparamagnetic nature with reduced size, small size, increased surface area to volume ratio, excellent dispersibility in solutions, reduced susceptibility to oxidation, magnetic stability, relatively easy synthesis, ease of surface modification, long blood retention time, biodegradability, and low toxicity.[7,8,10,11]

---

[a] *Inorganic Chemistry Laboratory, Department of Chemistry, National and Kapodistrian University of Athens, Panepistimiopolis, Zografou, 157 71, Greece. E-mail: efthim@chem.uoa.gr*

[b] *Department of Chemical Engineering, University of Patras, Caratheodory 1, Patras, GR, 265 04, Greece*

[c] *Institute of Nanoscience and Nanotechnology, NCSR "Demokritos", Aghia Paraskevi Attikis, 153 41, Greece*

[d] *Section of Condensed Matter Physics, Department of Physics, National and Kapodistrian University of Athens, Athens, 157 84, Greece*

[e] *Laboratory of Analytical Chemistry, Department of Chemistry, National and Kapodistrian University of Athens, Panepistimiopolis, Zografou, 157 71, Greece*

For instance, magnetic NPs as contrast agents present some positive characteristics, in contrast to conventional agents, such as shorter waiting time until examination, shorter duration of residence of the agent inside the patient's body (while reducing its side effects), and better detection of various tissue types, since they improve the overall image quality of the body's cells.[10,12,13] Depending on the size of the IONPs and the material used as a coating, they also target a different site for imaging. There are IONPs that have been approved for clinical use as magnetic resonance imaging (MRI) contrast agents; however, several of them have been already discontinued.[9,12]

When NPs consist of two different metals, they are called bimetallic. Bimetallic NPs (BNPs) are expected to have properties that are a combination of the properties of the two constituent metals, while they may also exhibit new properties that are a result of the synergy of the two metals. Their properties naturally differ from those of the pure elements, with the optical, electronic, thermal, and catalytic properties largely depending on the size of the formed NPs.[14,15] BNPs are an interesting field of research, as they add an additional degree of freedom due to the two different metals that compose them, resulting in different properties and, therefore, additional applications.[14,16–18] Nanomaterials doped with rare earth elements exhibit some exceptional chemical and optical characteristics, such as high photofluorescence intensity, long fluorescence lifetime, emission from the visible to near-ultraviolet spectrum, high stability against photochemical degradation, sharp emission peaks with a narrow bandwidth, constant light intensity, and low toxicity.[19–22] For the synthesis of these BNPs, two important features must be taken into account. First, lanthanide ions are characterized by a small molecular absorption cofactor, so that direct excitation does not always lead to strong fluorescence. This is corrected by the use of organic substituents (chromophores), which absorb light and transfer the energy to the excited states of the ions, which in turn exhibit fluorescence with a large Stokes shift. Second, since IONPs are known to be strong luminescence quenchers, it is necessary to coat the IONPs with a layer that suppresses the occurrence of this phenomenon. This coating also contributes to the immobilization of the lanthanides, improved chemical reactivity, and better colloidal stability of the NPs.[23–26]

Europium-doped iron oxide NPs (Eu-IONPs) have emerged as promising candidates, combining the superparamagnetic properties of iron oxides with the distinctive luminescent characteristics of europium ions. This dual functionality enables their use in multimodal imaging techniques, such as MRI and fluorescence imaging, enhancing diagnostic accuracy and therapeutic monitoring. Recent studies have focused on the synthesis and characterization of Eu-IONPs to optimize their physicochemical properties for biological applications.[27–33] For instance, Zhang *et al.*[31] reported the synthesis of biocompatible superparamagnetic Eu-IONP clusters using a straightforward one-pot method. These NPs exhibited excellent water solubility, colloidal stability, and enhanced T1-weighted MRI contrast, demonstrating their potential as multifunctional nanoprobes for *in vivo* imaging. Similarly, Costa *et al.*[32] developed hybrid magneto-luminescent iron oxide nanocubes functionalized with europium complexes. Their comprehensive evaluation of hemolytic properties and protein corona formation provided valuable insights into the biocompatibility and surface interactions of these NPs, which are crucial for their safe application in nanobiotechnology. Furthermore, Lunin *et al.*[33] introduced spindle-like Eu-IONPs synthesized through a facile ferrihydrite crystallization procedure. These NPs not only enhanced MRI contrast, but also exhibited shape-induced cytotoxicity, highlighting the influence of NP morphology on biological interactions and therapeutic potential. Two more groups, de Espindola *et al.*[34] and Prasad *et al.*,[35] highlighted the dual functionality of their NPs as a key feature enabling their potential applications. The combination of magnetic and optical properties allows for multimodal imaging and the possibility of simultaneous diagnosis and therapy (theranostics).

Building upon these advancements, our study aims to synthesize bimetallic Fe@Eu NPs with varying Fe : Eu ratios using the co-precipitation method. Structural, morphological, colloidal, and fluorescence properties were systematically characterized. *In vitro* assays, including cytotoxicity and cellular internalization, were performed to evaluate bioactivity. The synergistic interplay of iron and europium was shown to enhance multifunctionality, highlighting Fe@Eu NPs as promising platforms for biomedical imaging and therapeutic applications.

Experimental

Materials

Ferrous chloride ($FeCl_2 \cdot 4H_2O$) and ferric chloride ($FeCl_3 \cdot 6H_2O$) were purchased from Acros Organics. Ammonia solution (NH_4OH 30%; aquatic, Mr = 17.03 g mol^{-1}) and europium(III) nitrate pentahydrate ($Eu(NO_3)_3 \cdot 5H_2O$; Mr = 428.05 g mol^{-1}) were purchased from Sigma-Aldrich. Tri-sodium citrate ($Na_3C_6H_5O_7 \cdot 2H_2O$; Mr = 294.10 g mol^{-1}, d = 1.76 g cm^{-3}) was obtained from Fischer Scientific. Ethylene glycol ($C_2H_5O_2$; Mr = 62.07 g mol^{-1}, d = 1.11 kg L^{-1}) was obtained from Merck. Nitric acid (HNO_3, 65% G.R.; Mr = 63.01 g mol^{-1}, d = 1.4 kg L^{-1}) was purchased from Lach-Ner, s.r.o. High glucose DMEM (Dulbecco's Modified Eagle's Medium, with L-glutamine, with sodium pyruvate, sterile filtered), penicillin–streptomycin solution 100× (sterile filtered), L-glutamine 100× 200 mM (sterile filtered), and trypsin-EDTA 1× in solution (without Ca, without Mg, with phenol red, sterile filtered) were purchased from Biosera. DPBS (phosphate-buffered saline, without Ca, without Mg, sterile filtered) and FBS Good (fetal bovine serum) were obtained by PAN Biotech. MTT (3-(4,5-dimethylthiazol-2-yl)2,5-diphenyltetrazolium bromide) and PI (propidium iodide) were acquired from Cayman Chemical. RNAse A was obtained from abmGood. DMSO (dimethyl sulfoxide) was obtained from Fisher Chemical. DNR (daunorubicin hydrochloride) was provided by Pharmacia & Upjohn. Ethanol euro denatured 99% was purchased from VWR Chemicals. H_2DCFDA (2′,7′-dichlorodihydrofluorescein diacetate) was obtained from

Thermo Fisher Scientific. Annexin V binding buffer 10×, Annexin V/FITC (fluorescein isothiocyanate), and 7-AAD (7-aminoactinomycin D) were acquired from BD Biosciences.

Instrumentation

Dynamic light scattering (DLS) measurements of the samples were performed on a Malvern Instruments Zetasizer Nano Series with a multipurpose titrator. In the data presented in this study, each value represents the average value of 3 measurements, with 20 runs per measurement. The Fourier transform infrared (FT-IR) spectra of the samples were obtained using a Shimadzu IR Affinity-1 (QATR 10 single reflection ATR accessory) spectrometer and the spectra were scanned over the range 4000–400 cm^{-1}. The ultraviolet-visible (UV-Vis) absorption spectra in the wavelength range of 200–600 nm were obtained on a Shimadzu UV-2600i UV-Vis spectrophotometer. For the transmission electron microscopy (TEM) analysis, the images were taken using an FEI Talos F200i field-emission (scanning) transmission electron microscope (Thermo Fisher Scientific Inc., Waltham, MA, USA), operating at 200 kV and equipped with a windowless energy-dispersive spectroscopy microanalyzer (6T/100 Bruker, Hamburg, Germany). Photoluminescence (PL) spectra in the excitation/emission wavelength range of 300–900 were obtained using a Shimadzu RF-5301PC spectrofluorophotometer.

The powder X-ray diffraction (pXRD) spectra of the samples were obtained using a Bruker D8 Advance diffractometer in Bragg–Brentano geometry, operating at a voltage of 40 kV and a current of 25 mA. As an X-ray source, a Cu anode was used with Cu-Ka$_1$ radiation (λ = 1.5418 Å), while Cu-Ka$_2$ interferences are considered negligible due to the use of a Göbel mirror. Diffraction patterns were monitored in the 2θ angle range of 15–65 degrees with a step size equal to 0.04° s^{-1} and a scan speed equal to 1.6 s per step.

X-ray photoelectron spectroscopy (XPS) measurements were conducted within an ultra-high vacuum chamber at an operating pressure below 1.7×10^{-9} mbar.[36] A Leybold LH EA11 hemispherical energy analyzer, operated at 100 eV pass energy, was employed to analyze the kinetic energy of emitted photoelectrons excited by a non-monochromatic AlKα source emitting at 1486.6 eV. Sample powders were pressed against thin lead sheets and introduced into the chamber without further treatment. Spectra were analyzed using XPSPEAK 4.1 software, following the application of a Shirley background. The reported binding energies were charge-corrected with reference to adventitious carbon at 284.8 eV. Surface atomic ratios were calculated using experimental relative sensitivity factors.

The absorption of the solutions in the MTT assay was measured on an Eliza Microplate Reader Biobase spectrophotometer; the test wavelength was set at 540 nm and the reference wavelength at 620 nm. Widefield optical fluorescence microscopy of the NPs was carried out using an OMAX Trinocular Compound EPI-fluorescence microscope (model: M834FLR) with a 1.3 MP CMOS camera (blue filters: excitation 410–490 nm, emission 515 nm; green filters: excitation 490–540 nm, emission 590 nm), while for cells it was carried out using a EUROMEX bScope Trino Plan Fluo Microscope (model: BS.3153-PLI) with a 6.1 MP 1/1.8'' SONY EXMOR CMOS SENSOR Euromex Scientific Camera (sCMEX-6) (blue filters: excitation 450–495 nm, emission 515; green filters: excitation 495–555 nm, emission 595 nm; violet filters: excitation 380–415 nm, emission 475 nm; ultraviolet filters: excitation 320–380 nm, emission 435 nm). Intracellular iron and Europium quantification was performed *via* inductively coupled plasma-mass spectrometry using an Agilent 7900 ICP-MS instrument. Helium was used as the collision gas to minimise polyatomic interferences, and the isotopes used for quantification were 56Fe and 151Eu.The flow cytometry experiments were conducted on a Becton Dickinson FACSCalibur flow cytometer and the obtained data were processed using FlowJo software.

Synthetic procedures

Synthesis of magnetic iron oxide nanoparticles (IONPs). The synthesis of IONPs was based on the work of Prokopiou *et al.*[37] In a 250 mL round bottom flask, placed inside an oil bath and on a heated stirrer, 80 mL of double distilled (dd.) water was added. The flask was heated at around 70 °C for 30 min in the presence of bubbling N_2 gas. The presence of N_2 gas prevents the oxidation of iron, which is added later in the reaction flask, to γ-Fe_2O_3 (reaction (R1)) or $Fe(OH)_3$ (reaction (R2)). After 30 min, 0.5 g (2.5 mmol) $FeCl_2{\cdot}4H_2O$ and 1 g (6.2 mmol) $FeCl_3{\cdot}6H_2O$ were added into the reaction flask; according to studies, an Fe(II) : Fe(III) ratio of 1 : 2 contributes to the formation of iron oxide nuclei, which consist of magnetite at a percentage higher than 95%. After the temperature reached 90 °C and the two salts were solubilized, 8 mL of concentrated ammonia solution (NH_3) was added into the flask to ensure the alkaline environment needed for the formation and precipitation of magnetite. At the end of the reaction, the color of the mixture turned black, indicating the formation of magnetite. When the reaction mixture cooled down to room temperature, the precipitate was magnetically separated and washed thrice with dd. water, in order to remove excess reagents. The synthesized magnetic IONPs were dispersed in water and stored at 4 °C. The overall reaction of the synthesis is presented below (reaction (R3)).[38]

$$Fe_3O_4 + 2H^+ \rightarrow \gamma\text{-}Fe_2O_3 + Fe^{2+} + H_2O \qquad (R1)$$

$$Fe_3O_4 + \frac{1}{4}O_2 + \frac{9}{2}H_2O \rightarrow 3Fe(OH)_3 \qquad (R2)$$

$$2Fe^{3+} + Fe^{2+} + 8OH^- \rightarrow Fe_3O_4 + 4H_2O \qquad (R3)$$

Synthesis of magnetic IONPs coated with tri-sodium citrate (IONPs@citrate). This synthesis was based on the work of Prokopiou *et al.*[37] with some modifications. In a 100 mL round bottom flask, placed inside an oil bath and on a heated stirrer, 40 mL of dd. water was added. The flask was heated at around 80 °C for 30 min in the presence of bubbling N_2 gas. After 30 min and at the same temperature, 0.5 g (2.5 mmol) $FeCl_2{\cdot}4H_2O$ and 1 g (6.2 mmol) $FeCl_3{\cdot}6H_2O$ were added into the reaction flask with an Fe(II) : Fe(III) ratio of 1 : 2 and the mixture was left until complete dissolution. After the dissolution of the salts and while the temperature was still at 80 °C, 2.5 mL of concentrated ammonia solution (NH_3) was added into the reaction flask. At this stage, 1 g (3.4 mmol) tri-sodium citrate was dissolved in 2 mL of distilled water and added into the reaction flask after another 30 min. The addition of tri-sodium citrate was followed by an increase in temperature (95 °C) and the reaction was left to complete for 90 min. When the reaction mixture cooled down to room temperature, the precipitate was magnetically separated and washed thrice with dd. water. The synthesized magnetic IONPs@citrate was dispersed in water and stored at 4 °C. The overall reaction of the synthesis is presented below (reaction (R4)).[39]

$$\begin{gathered}2FeCl_3 + FeCl_2 + 8NH_3 + 4H_2O \\ + (HOOC)(CH_2)C(OH)(COOH)(CH_2)(COOH) \\ \rightarrow \text{citrate} - Fe_3O_4 + 8NH_4Cl \qquad (R4)\end{gathered}$$

Each molecule of citric acid has three carboxyl groups (–COOH) in its structure, from which one or two are adsorbed on the surface of the IONPs by chemisorption. In a wide pH range (5.0–9.0), due to the three pK_a values, citric acid undergoes strong deprotonation (–COOH → $-COO^-$), which contributes to the strong negative charge on the surface of IONPs and the strong electrostatic repulsion. In this way, the colloidal stability of the magnetic IONPs in aquatic systems is enhanced and agglomeration is avoided.[39]

Syntheses of magnetic IONPs coated with tri-sodium citrate and modified with europium with Fe : Eu ratios of 1 : 3, 1 : 1, and 1 : 0.25 having water as the dispersion medium (IONPs@citrate@Eu (Fe : Eu = 1 : 3, in H_2O), IONPs@citrate@Eu (Fe : Eu = 1 : 1, in H_2O), IONPs@citrate@Eu (Fe : Eu = 1 : 0.25, in H_2O)). These syntheses were based on the work of Espindola *et al.*[34] with some modifications. Particularly, in the case of an Fe : Eu ratio of 1 : 3, in a 50 mL round bottom flask, placed inside an oil bath and on a heated stirrer, 20 mL of dd. water was added. The flask was heated at around 70 °C in the presence of bubbling N_2 gas. Then, 870 μL of IONPs@citrate was added into the flask and after 10 min 2–3 drops of concentrated ammonia solution (NH_3) was added as well. Ammonia contributes to the alkaline environment needed for deprotonation of the carboxyl groups of citrate on the IONPs' surface (–COOH → $-COO^-$), so that europium can be more easily attached to them. After another 10–15 min, 0.15 g (0.35 mmol) $Eu(NO_3)_3\cdot 5H_2O$ (Fe : Eu ratio = 1 : 3) was added into the reaction flask and the reaction was left to complete for 24 h. When the reaction mixture cooled down to room temperature, the precipitate was magnetically separated and washed thrice with dd. water. The synthesized magnetic IONPs@citrate@Eu (Fe : Eu = 1 : 3, in H_2O) were dispersed in water and stored at 4 °C.

Similar procedures were followed for the syntheses of the magnetic IONPs@citrate@Eu with Fe : Eu ratios of 1 : 1 and 1 : 0.25. However, for these two ratios, 750 μL of concentrated ammonia was added for the deprotonation of citrate molecules and the reactions were completed after 2 h. Moreover, for sample IONPs@citrate@Eu (Fe : Eu = 1 : 1, in H_2O), the amount of added $Eu(NO_3)_3\cdot 5H_2O$ was 0.054 g (0.13 mmol), whilst for sample IONPs@citrate@Eu (Fe : Eu = 1 : 0.25, in H_2O) the amount was 0.014 g (0.033 mmol).

Syntheses of magnetic IONPs coated with tri-sodium citrate and modified with europium with Fe : Eu ratios of 1 : 1 and 1 : 0.25 having ethylene glycol as the dispersion medium (IONPs@citrate@Eu (Fe : Eu = 1 : 1, in EG), IONPs@citrate@Eu (Fe : Eu = 1 : 0.25, in EG)). These syntheses were based on the work of Martinson *et al.*[40] with some modifications. Particularly, in the case of an Fe : Eu ratio of 1 : 1, in a 25 mL round bottom flask, placed inside an oil bath and on a heated stirrer, 10 mL of ethylene glycol (EG) was added. The flask was heated at around 80 °C in the presence of bubbling N_2 gas. Then, 435 μL of IONPs@citrate and 200 μL of NaOH 1 N were added into the flask. In this case, NaOH was used instead of NH_3 for the deprotonation of the carboxyl groups of citrate molecules on the IONPs' surface. After 30 min, 0.027 g (0.063 mmol) $Eu(NO_3)_3\cdot 5H_2O$ dissolved in 500 μL ethanol (EtOH) was added into the reaction flask and the reaction was left to complete for 2 h. When the reaction mixture cooled down to room temperature, the precipitate was magnetically separated and washed thrice with dd. water. The synthesized magnetic IONPs@citrate@Eu (Fe : Eu = 1 : 1, in EG) were dispersed in water and stored at 4 °C.

The same procedure was followed for the synthesis of the magnetic IONPs@citrate@Eu with an Fe : Eu ratio of 1 : 0.25. Nevertheless, in this case, the amount of added $Eu(NO_3)_3\cdot 5H_2O$ was equal to 0.0068 g (0.016 mmol).

Ethylene glycol, with its two hydroxyl groups, serves as an effective complexing agent for metal ions of varying sizes. Its use in synthesis helps prevent selective precipitation and ensures better homogeneity among components. In the presence of nitrate anions, a phenomenon known as the ''glycol effect'' occurs.[41] Nitrates tend to form strong hydrogen bonds with ethylene glycol in the polar domain, dominating its coordination sphere and reducing interactions with other ions.[42] This interaction also initiates an exothermic redox reaction between nitrate and the hydroxyl groups, producing nitrogen oxide gases (NO_x) and oxidizing ethylene glycol to glyoxylate.[43] In this study, ethylene glycol was used specifically to minimize the disruptive effects of nitrate ions during NP synthesis.

All syntheses were performed *via* a one-pot co-precipitation process.

In vitro biological evaluation

Cell culture. Human embryonic kidney (HEK-293) and Henrietta Lacks (HeLa) cells were, respectively, the healthy and cancerous cell lines used in this study. Both cell lines were cultured and maintained in glutamine-rich DMEM supplemented with 10% FBS and 1% penicillin/streptomycin as antibiotics. The cell cultures were incubated at 37 °C with 5% CO_2 flow inside a humidified incubator.

MTT cell viability assay. Initially, HEK-293 and HeLa cells were seeded in 96-well plates at a cell density of 1×10^4 cells per well and incubated for 24 h until confluency. To achieve different concentrations of the synthesized NPs in DMEM, stock solutions were prepared followed by serial dilutions, resulting in final concentrations of 100, 50, 30, 10, 5, and 1 μM Fe. After a 24 h incubation, the culture medium was removed and replaced by DMEM containing the different concentrations in triplicate. After another 24 h of incubation with the NPs, the medium was removed and replaced by the MTT solution (0.5 mg mL^{-1} in PBS). After 1–3 h of incubation with MTT, dark purple formazan crystals precipitated at the bottom of the wells, indicating the presence of living cells. The formazan crystals were dissolved upon the addition of DMSO and the absorbance was measured at 540 nm (reference wavelength at 620 nm) with an ELISA plate reader.[44] The percentage (%) of the viable cells can be calculated using the following equation (eqn (1)):

$$\%\ \text{Cell viability} = \frac{\text{Number of stained cells}}{\text{Total number of cells}} \times 100\% \qquad (1)$$

Wound healing assay. The migratory potential and multiplicative capacity of the cells, both HEK-293 and HeLa, were assessed using the wound healing assay. According to this method, the cells were seeded in 24-well plates in DMEM at a cell density of 5×10^4 cells per well and incubated until confluency. A straight scratch was made in the confluent monolayer using a p200 pipette tip and detached cells were removed by washing with PBS. Some wells of the plate were treated only with DMEM, in order to serve as the control, and the rest were treated with NPs with a concentration of 100 μM_{Fe} dispersed in DMEM. The scratched areas of each sample and the controls were photographed at the time points of 0 h, 24 h, 48 h, and 72 h for HEK-293 cells and at 0 h, 24 h, and 28 h for HeLa cells with a 1.3 MP CMOS camera. The images that were taken at different time points were processed using the ImageJ program, which determined the denuded cell area. The percentage (%) of the healed wound at the different time points can be calculated using the following equation (eqn (2)):

$$\%\ \text{Wound closure} = \left(\frac{\text{Initial wound size} - \text{Final wound size}}{\text{Initial wound size}}\right) \times 100\% \qquad (2)$$

where the initial wound size is the one at 0 h and the final wound size is the one at the different time points.[45]

Prussian blue staining and optical microscopy. This method is commonly used to visualize the cellular uptake of NPs and is based on the formation of the insoluble blue complex $\mathrm{Fe(III)_4[Fe(II)(CN)_6]_3 \cdot \mathit{x}H_2O}$, known as Prussian blue. Briefly, cells were seeded in 12-well plates at a density of 1×10^5 cells per well and incubated until reaching confluency. Subsequently, the culture medium was removed and replaced with fresh DMEM for control samples and with DMEM containing NPs at a concentration of 100 μM_{Fe} for treated samples. After 24 hours of incubation, the medium was discarded and cells were washed with PBS and fixated with 4% formalin for 20 min at room temperature. Following fixation, cells were washed twice with PBS and treated with Pearl's solution – a 1 : 1 mixture of 4% (w/v) potassium ferrocyanide ($K_4Fe(CN)_6 \cdot 3H_2O$) and 4 M HCl in PBS – for 30 min at room temperature. The acidic environment promotes partial dissolution of the internalized NPs by providing protons, which liberate Fe(III) ions from the NP matrix. These free Fe(III) ions subsequently react with ferrocyanide to form the characteristic Prussian blue complex, marking the sites of iron accumulation within the cells. After the staining procedure, cells were rinsed with PBS and counterstained with 0.02% nuclear red solution for at least 5 min to visualize cell nuclei, which appear red and provide contrast against the blue-stained regions indicating iron presence. Finally, the cells were washed again with PBS, imaged under an optical microscope, and documented using a 1.3MP CMOS camera.[44]

Fluorescence microscopy in cells. This technique contributes, as well, to the visualization of the NPs' uptake by the cells and was used to locate the spot of the NPs in the cells due to the fluorescence of europium. To begin with, the cells were seeded in 24-well plates containing sterile coverslips at a cell density of 5×10^4 cells per well and incubated until confluency. After the incubation, the culture medium was removed and DMEM was added to the control wells and NPs with a concentration of 100 μM_{Fe} dispersed in DMEM were added to the sample wells. After another 24 h, the medium was removed, and the cells were washed with PBS, fixated with 4% formalin for 20 min at room temperature, and washed again with PBS. Finally, the coverslips were removed and placed on glass slides to perform fluorescence microscopy. The cells were photographed with a 6.1 MP 1/1.8″ SONY EXMOR CMOS SENSOR Euromex Scientific Camera (model: sCMEX-6).

Study of the cell cycle by flow cytometry. The protocol followed was based on the work of Kim *et al.*[46] with minor modifications. Briefly, cells were seeded in 6-well plates at a density of 3×10^5 cells per well until reaching confluency. The culture medium was then replaced with DMEM for the negative controls, with DMEM containing 1 μg mL^{-1} daunorubicin hydrochloride (DNR) for the positive controls, and with DMEM containing Fe@Eu NPs at a concentration of 100 μM_{Fe} for the treated groups. After 24 h of incubation, the medium was removed, and the cells were washed with PBS and harvested. Cells were subsequently fixated in 70% (v/v) cold ethanol in water for 1 h in the dark and stored overnight at 4 °C. Cells were washed with PBS and incubated for 30 min in the dark with 500 μL PI/RNAse A (50 μg mL^{-1} PI and 10 μg mL^{-1} RNAse A in PBS). PI is a red fluorescent stain (λ_{ex} = 535 nm, λ_{em} = 617 nm) with binding efficiency to both DNA and RNA, while RNAse A is necessitated to be used in order to digest the double-stranded sections of RNA and confirm that only DNA is stained by the PI.[47] Flow cytometry was then performed to assess the cell distribution percentages (%) in the sub-G1, G1, S, G2, and post-G2 phases. The cells were analyzed using a FACSCalibur flow cytometer and data were processed using FlowJo software.

Study of the intracellular production of reactive oxygen species (ROS) by flow cytometry. The protocol followed was adapted from the work of Pérez-Arizti *et al.*[48] with minor modifications. Briefly, cells were seeded in 6-well plates at a density of 3×10^5 cells per well and incubated until reaching confluency. The medium was then replaced by DMEM for the negative controls and by NPs with a concentration of 100 μM_{Fe} dispersed in DMEM for the rest. After 24 h of incubation, the medium was removed, and cells were washed with PBS and harvested. After another wash with PBS, and cells were incubated with 10 μM H_2DCFDA in DMEM (not supplemented with FBS) for 30 min at 37 °C in the dark, and subsequently washed twice with PBS. After the entrance of cell-permeable and non-fluorescent H_2DCFDA inside the cell, it is converted into 2′,7′-dichlorofluorescein (DCF), the oxidized and highly fluorescent form (excitation at 485 nm, emission at 530 nm),[49] presenting the redox state of the sample.[50,51] ROS levels were assessed using a FACSCalibur flow cytometer. A minimum of 10 000 events per sample were analyzed using FlowJo software.

Study of the apoptotic and necrotic pathways by flow cytometry. The protocol followed was based on the work of Pedrino *et al.*[52] with some modifications. Briefly, cells were seeded in 6-well plates at a density of 3×10^5 cells per well and incubated until reaching confluency. The culture medium was then removed and replaced with fresh DMEM for the negative control group or with DMEM containing NPs at a concentration of 100 μM_{Fe} for the treated groups. After 24 h of incubation, the medium was discarded, and cells were washed with PBS and subsequently harvested. Following collection, cells were washed once again with PBS and 100 μL of 1× binding buffer was added to each sample. Cells were then stained with 5 μL of Annexin V/FITC and 5 μL of 7-AAD and incubated in the dark for 20 min at room temperature. The Annexin V/FITC complex (λ_{ex} = 490 nm, λ_{em} = 525 nm) binds to phosphatidylserine (PS), a membrane component that becomes externalized on the cell surface during early apoptosis and allows for the identification of apoptotic cells with intact membranes. In contrast, 7-AAD (λ_{ex} = 488 nm, λ_{em} = 647 nm) is a DNA-intercalating dye that can only permeate cells with compromised membranes, thereby labeling necrotic and late apoptotic cells.[53–55] After staining, an additional 400 μL of 1× binding buffer was added to each sample and flow cytometry was performed to quantify the percentages of viable, early apoptotic, late apoptotic, and necrotic cells. Cell analysis was conducted using a FACSCalibur flow cytometer and data were acquired from a minimum of 10 000 events per sample. The resulting data were further processed and analyzed using FlowJo software.

Quantification of intracellular iron and europium in cultured cells *via* ICP-MS. Cells were prepared for ICP-MS measurement following modified methods described previously.[56,57] Comprehensively, cells were seeded in 6-well plates until reaching confluency, after which the culture medium was replaced by fresh DMEM for the control groups (quantification of endogenous iron in cells) and by NPs with a concentration of 100 μM_{Fe} for the rest. After 24 h of incubation, the medium was removed, and cells were washed twice with PBS in order to completely remove the extracellular NPs and harvested. Subsequently, cells were washed twice with PBS, treated with 1 mL of 65% HNO_3, and left for 2 h in an oil bath at 90 °C until complete digestion. In order to prevent pressure buildup, vial caps were kept slightly open during digestion. The procedure was also carried out in a chemical fume hood to ensure safe handling of vapors, particularly due to the possible release of nitrogen oxides (NO_x) generated during the oxidative decomposition of cellular material. The digestion process was carried out in vials that were thoroughly rinsed with dd. water and 2% HNO_3 prior to use. Following digestion, the samples were allowed to cool to room temperature and then diluted with dd. water to a final solution containing 2% HNO_3. Eight-point calibration curves for iron and europium were performed prior to sample analysis based on standard solutions prepared at 0, 1, 2.5, 5, 10, 25, 50, and 100 ppb in 2% HNO_3. Total iron and europium content per cell was calculated based on the calibration curves and known cell number.

Statistical analysis. The results of the *in vitro* biological evaluation are expressed as the mean value of three independent experiments ± SD (standard deviation of the average value). For the statistical analysis of the MTT, ROS, and ICP-MS data, ordinary two-way ANOVA was carried out, followed by Tukey's multiple comparisons test, with individual variances computed for each comparison. For the statistical analysis of the cell cycle and apoptosis/necrosis data, ordinary two-way ANOVA was carried out, followed by Dunnett's multiple comparisons test, with individual variances computed for each comparison. Statistical significance was declared for *p* values less than 0.05 (95% confidence interval). Statistical analysis was performed using GraphPad Prism 9.0.0 software.

Results and discussion

Structural and morphological characterization

UV-Vis spectroscopy. It is well established that the absorption spectra of iron compounds present three main peaks corresponding to three types of electronic transitions. Firstly, at low energy, Fe^{3+} d–d transitions and pair excitation processes are in charge. As for d–d transitions, electrons from the highest spin multiplicity state (ground state at lower energy) transition to a lower spin multiplicity state. Pair excitation, also known as double excitation, is a phenomenon that occurs due to magnetic coupling between two neighboring Fe^{3+} ions, resulting in their simultaneous excitation. Secondly, at medium energies, ligand-to-metal charge-transfer (LMCT) transitions are observed. In this type of transition, O^{2-} is the ligand that is responsible for the strong absorption below 400 nm. Lastly, at high energies, intraligand (IL) transitions take place. These types of transitions are due to the magnetic coupling of two adjacent Fe^{3+} ions and they result in hybridization or overlapping between the 3d orbitals of Fe and the 2p orbitals of O.[2,58] The transposition of the LMCT peak can give important information about the size of the NPs. A decrease in particle size generally leads to a blueshift of this peak, while an increase in size results in a redshift. Moreover, it is important to clarify that magnetite can strongly absorb light in the wavelength range of 250–900 nm, making it difficult to distinguish the different transitions in the spectra.[58]

The UV-Vis spectra of each synthesis are presented in Fig. S1 of the SI. In all the absorption spectra of the NPs, three major

Table 1 Summary of the D_H (nm), PdI, and ZP (mV) values for each synthesis. The presented data are the average of three measurements ± standard deviation (SD)

Sample	D_H (nm)	PdI	ZP (mV)
IONPs	1.038 ± 74.32	0.644 ± 0.032	−44.1 ± 2.21
IONPs@citrate	221.9 ± 2.691	0.329 ± 0.018	−40.6 ± 0.709
IONPs@citrate@Eu (Fe : Eu = 1 : 3, in H_2O)	993.2 ± 50.71	0.510 ± 0.027	24.2 ± 0.702
IONPs@citrate@Eu (Fe : Eu = 1 : 1, in H_2O)	2.156 ± 178.4	0.693 ± 0.062	34.9 ± 0.503
IONPs@citrate@Eu (Fe : Eu = 1 : 1, in EG)	2.964 ± 809.5	0.744 ± 0.183	39.7 ± 0.404
IONPs@citrate@Eu (Fe : Eu = 1 : 0.25, in H_2O)	2.553 ± 382.3	0.835 ± 0.084	9.20 ± 1.13
IONPs@citrate@Eu (Fe : Eu = 1 : 0.25, in EG)	2.448 ± 462.4	0.719 ± 0.110	14.3 ± 0.854

peaks are observed. The first peak around 200 nm is attributed to IL transitions, the second peak around 380 nm is attributed to LMCT transitions, and the third peak around 490 nm is attributed to d–d or pair excitation processes. Among the three observed peaks, the one corresponding to LMCT transitions is the most clearly observed, giving important information about the structure of the NPs, and the one corresponding to d–d or pair excitation processes is the least clearly observed, probably due to overlapping with LMCT transitions. Based on the theory that the LMCT peak blueshifts with reducing size and redshifts with increasing size of the NPs, we can draw two major conclusions. Firstly, the addition of tri-sodium citrate redshifts the spectrum, indicating the attachment on the IONPs' surface and resulting in NPs of bigger size. Secondly, the addition of europium results in Fe@Eu NPs of either a slightly bigger or a slightly smaller size. This indicates that europium managed to be incorporated in IONPs@citrate, but probably changes its structure. No characteristic absorption peak due to europium is observed in the spectra, since, as already mentioned, magnetite strongly absorbs light in the wavelength range of 250–900 nm. However, analysis of the UV-Vis spectra reveals that a lower theoretical europium content in the Fe@Eu NPs corresponds to reduced absorption intensity.

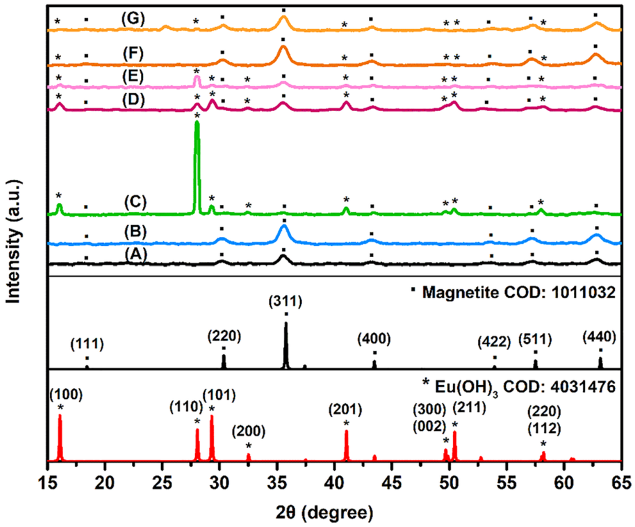

Fig. 1 pXRD patterns of the synthesized NPs. Peaks were smoothed using OriginPro 9.0. NPs: (A) IONPs, (B) IONPs@citrate, (C) IONPs@citrate@Eu (Fe : Eu = 1 : 3, in H_2O), (D) IONPs@citrate@Eu (Fe : Eu = 1 : 1, in H_2O), (E) IONPs@citrate@Eu (Fe : Eu = 1 : 1, in EG), (F) IONPs@citrate@Eu (Fe : Eu = 1 : 0.25, in H_2O), and (G) IONPs@citrate@Eu (Fe : Eu = 1 : 0.25, in EG).

DLS measurements. This technique is commonly used to determine the hydrodynamic diameter (D_H) and zeta potential (ZP) of spherical NPs in colloidal dispersions. D_H represents the diameter of NPs including the surrounding solvent layer, making the measurement indicative rather than exact. ZP is a measurement that gives important information about the colloidal stability and the state of agglomeration.[59–62]

Table 1 summarizes the DLS characteristics of the synthesized NPs (distribution curves of size and ZP are shown in Fig. S2 of the SI). The data indicate that varying the europium content in Fe@Eu NPs influences their colloidal stability. Specifically, IONPs, IONPs@citrate, and IONPs@citrate@Eu with an Fe : Eu ratio of 1 : 1 (synthesized in H_2O and in EG) exhibit good colloidal stability since ZP is |30–50| mV. In contrast, IONPs@citrate@Eu with Fe : Eu ratios of 1 : 3 (synthesized in H_2O) and 1 : 0.25 (synthesized in H_2O and in EG) are characterized by aggregation, thus reducing the colloidal stability. These observations regarding the Fe@Eu NPs are visually supported and align with experimental results. Across all samples, the D_H and PdI values are increased, indicating a tendency for NP aggregation. However, the exact size of the Fe@Eu NPs will be further characterized using TEM and pXRD analyses.

FT-IR spectroscopy. The FT-IR spectra of the synthesized NPs are displayed in Fig. S3 of the SI. The high intensity peaks observed around 540–550 cm^{-1} in all spectra are attributed to the presence of Fe–O–Fe bonds in magnetite. Particularly, these peaks correspond to the strain vibration of the iron atoms occupying the tetrahedral sites in the crystal structure.[63] The absorption peaks around 1590 and 1370 cm^{-1} can be attributed to the asymmetric stretching vibration of the carbonyl group (–C=O) and the symmetrical stretching vibration of the carboxylic anions (–COO$^-$) of citrate, respectively.[64] Especially, the second peak might be an indication of the presence of a –COO–Fe bond, which is attributed to the reaction between the hydroxyl radicals on magnetite's surface and the carboxylic groups of citrate.[65] With the addition of europium on the NPs' surface, these two peaks show a slight shift. Apart from supporting the presence of the chemisorbed carboxylate groups of citrate on the NPs, according to the literature, these two peaks give information about the way citrate molecules bind to the magnetite surface.[64] When the mathematical difference of these two peaks is bigger than 200 cm^{-1}, the carboxylic acids form monodendate binding with the magnetite surface and, when the difference is smaller than 200 cm^{-1}, the binding is bidendate.[66] According to this, citrate anions form monodendate binding only in the IONPs@citrate sample, whereas in all IONPs@citrate@Eu samples the binding is bidendate. The peaks at 3605 and 3610 cm^{-1} are of particular interest, because, according to the literature, they are attributed to the presence of $Eu(OH)_3$ rods.[67]

pXRD analysis. The pXRD patterns and the corresponding *hkl* indexes are displayed in Fig. 1, demonstrating a complex structural fingerprint. Across all samples, key diffraction peaks corresponding to magnetite – (111), (220), (311), (400), (422), (511), and (440) – match well with the standard magnetite reference (COD ID: 1011032), confirming the presence of an inverse spinel structure (space group: *Fd*3*m*, face-centered cubic lattice).[27,68] According to the literature, the difference in the intensity among the syntheses, during europium addition, indicates that crystallinity and crystallite particle size differ, while magnetite formation remains stable.[68] The relatively broad and weak peaks hint at low crystallinity or possible impurity phases.[69] On the other hand, it is demonstrated that the addition of europium into the magnetic NPs' lattice leads to magnetite diffraction peaks of lower intensity as well as the appearance of some extra intense peaks, suggesting more than just structural distortion. This might mean that the addition of europium either inhibits the growth of the NPs or disrupts the network to which it is added, resulting in a change in crystallinity.[70] Usually, the presence of comparatively more intense peaks indicates the presence of a different phase in the sample.[71] This hypothesis is supported by the FT-IR results, indicating the presence of $Eu(OH)_3$ nanorods, while their presence is confirmed by comparing the diffraction peaks to the literature. In particular, comparing the diffraction patterns of the samples with the standard for $Eu(OH)_3$ nanorods (COD ID: 4031476), it can be observed that crystalline planes (100), (110), (101), (200), (201), (300), (002), (211), (220), and (112) are present in almost all cases.[67] The specific diffraction peaks become more intense when increasing the amount of europium added into the magnetic NPs and indicate the presence of a hexagonal lattice (space group *P*63/*m*).

The formation of $Eu(OH)_3$ is probably driven by the alkaline conditions during the addition of europium nitrate. It is well established that amines and ammonia promote the precipitation of trivalent rare-earth hydroxides[72] according to the following reaction (reaction (R5)):

$$Eu^{3+}(aq) + 3H_2O \xrightarrow{NH_3(aq)} Eu(OH)_3(s) + 3H^+(aq) + NH_4^+(aq) \quad (R5)$$

Based on these results, we hypothesize that a small amount of europium is either incorporated into the magnetite lattice or adsorbed onto the surface of the NPs. This is likely driven by electrostatic interactions between the positively charged Eu^{3+} ions and the negatively charged surface of citrate-coated iron oxide NPs (IONPs@citrate). Considering the fact that the ionic radii of europium ions are almost twice those of iron ions and high temperatures are not applied, it is likely that the incorporation of trivalent lanthanide ions is governed by kinetic factors. In terms of nanomaterials, the lattice of the synthesized crystals could contain defects as a result of the kinetically "frozen" crystal growth in cases of non-thermodynamic equilibrium. The defects present in the lattice could lead to exchanges of cationic species or incorporation of ions of different valences. Except from the lattice, defects can also be formed on the surface of the nanocrystals favoring the stabilization of molecules, even solvent molecules.[73]

Table 2 Summary of the variations in crystallite size, *D* (nm), and strain, ε, between each synthesis

Sample	*D* (nm)	ε (×10^{-3})
IONPs	8.86	4.34
IONPs@citrate	8.31	4.37
IONPs@citrate@Eu (Fe : Eu = 1 : 3, in H_2O)	11.14	3.57
IONPs@citrate@Eu (Fe : Eu = 1 : 1, in H_2O)	8.06	4.82
IONPs@citrate@Eu (Fe : Eu = 1 : 1, in EG)	9.32	4.34
IONPs@citrate@Eu (Fe : Eu = 1 : 0.25, in H_2O)	8.51	4.27
IONPs@citrate@Eu (Fe : Eu = 1 : 0.25, in EG)	8.77	4.24

X-ray diffraction measurements contribute to the determination of the average crystallite size of the synthesized NPs. The size is calculated using the Debye–Scherrer equation (eqn (3)):

$$D = 0.9\frac{\lambda}{\beta\cos\theta} \quad (3)$$

where *D* is the average crystallite size of the NPs, λ is the wavelength of the used X-rays (1.5418 Å), β represents the Bragg peak's full width at half maximum (FWHM), and θ is the Bragg's diffraction angle.[68] When larger Eu ions replace smaller Fe ions in the magnetite lattice, defects and vacancies are formed, leading to lattice strain. The microstrain (ε) of the lattice can be calculated using eqn (4):[74]

$$\varepsilon = \frac{\beta\cos\theta}{4} \quad (4)$$

Table 2 presents the alterations of the crystallite size and the respective strain among the different synthesized NPs. Mathematically, crystallite size (*D*) and lattice strain (ε) are two inversely proportional quantities and a decrease in one implies an increase in the other. Theoretically, a reduction of crystallite size indicates a compression of the lattice and the unit cell, which in turn leads to elevation of the internal stress and, thus, the strain. The induced stress of the lattice can be either internal type or surface type. For instance, elevated strain can be observed in cases where smaller ions are substituted by larger ones in the crystal lattice.[75]

Analyzing the data in Table 2 and comparing the Fe@Eu NPs with IONPs@citrate, it can be seen that, in some cases, *D* is increased and accompanied by a decreased ε, while, in others, the exact opposite is observed. The elevation or reduction of these values does not appear to have any specific correlation to the amount of europium present in the Fe@Eu NPs. This means that larger europium ions substitute smaller iron ions in the magnetite lattice or they are incorporated in the defects

Table 3 Elemental analysis (atomic ratios of the different species on the surface of the NPs) of the samples conducted by XPS

Sample	Eu/Fe[a]	Eu/O[b]	Fe/O[c]	Fe^{3+}/Fe^{2+}	O $(M–O_x)$/O (M–OH)[d]
IONPs@citrate	n.a.	n.a.	0.44	2.26	2.94
IONPs@citrate@Eu (Fe : Eu = 1 : 3, in H_2O)	4.44	0.82	0.18	2.94	0.62
IONPs@citrate@Eu (Fe : Eu = 1 : 1, in H_2O)	3.88	0.65	0.17	2.80	0.79
IONPs@citrate@Eu (Fe : Eu = 1 : 0.25, in H_2O)	1.80	0.54	0.30	2.62	1.76

[a] Surface atomic ratio of europium and iron. [b] Surface atomic ratio of europium and oxygen. [c] Surface atomic ratio of iron and oxygen. [d] Ratio of peaks belonging to metal oxide species $(M–O_x)$ and hydroxide and metal hydroxide species (M–OH, –OH) in the O 1s region.

formed internally or on the surface of the lattice. Probably, these alterations of the crystal lattice are not arranged in a consistent order, but rather randomly.

XPS analysis. XPS was performed for the determination of the composition of the synthesized NPs and the determination of the various oxidation states of the elements present in the NPs. Herein, IONPs@citrate as a standard sample and IONPs@citrate@Eu (Fe : Eu = 1 : 3, 1 : 1, and 1 : 0.25, in H_2O) are representative examples. XPS scans of the samples revealed the presence of Eu, Fe, O, and C. In general, the XPS data show the presence of magnetite in all samples and its coexistence with $Eu(OH)_3$ in samples IONPs@citrate@Eu with Fe : Eu ratios of 1 : 3, 1 : 1, and 1 : 0.25 in H_2O. Apart from the Eu 3d region, the O 1s region is also in very good agreement with the above findings (Table 3).

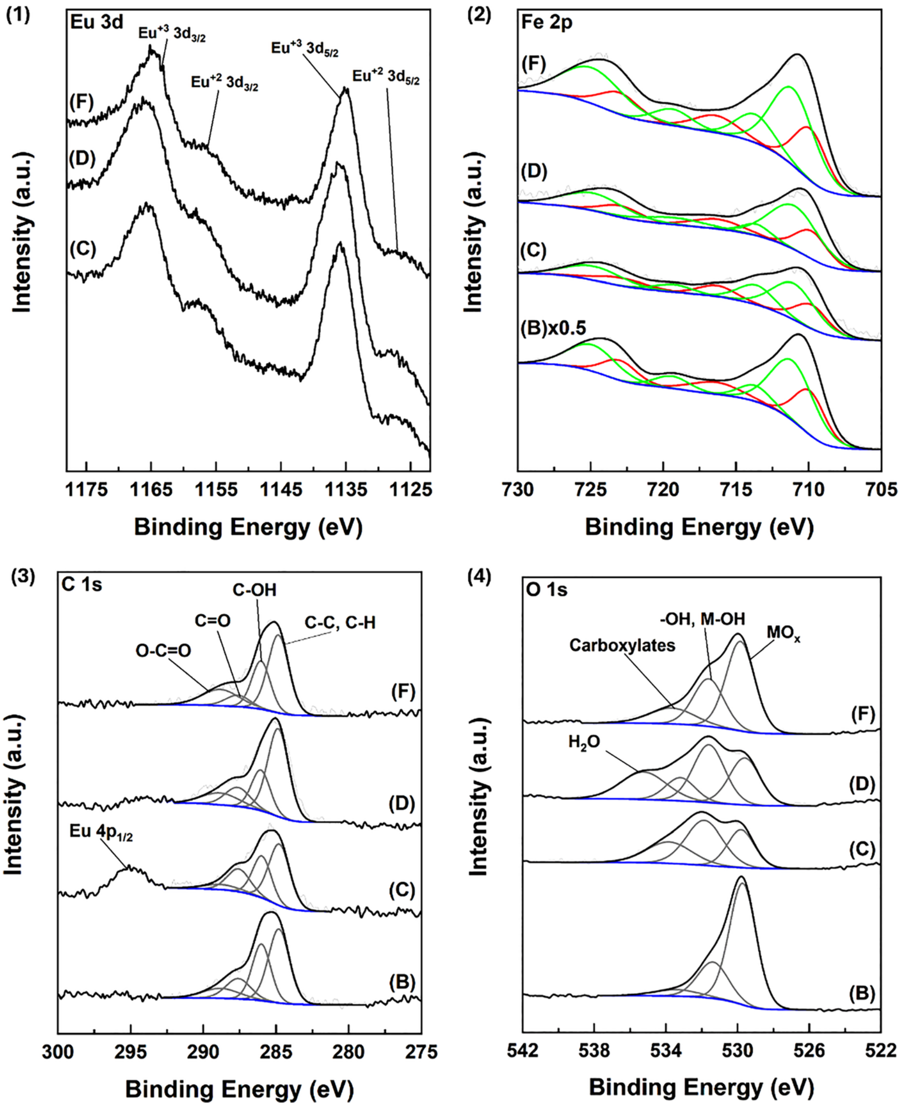

Fig. 2 XPS spectra of (1) Eu 3d, (2) Fe 2p, (3) C 1s, and (4) O 1s for the samples (B) IONPs@citrate, (C) IONPs@citrate@Eu (Fe : Eu = 1 : 3, in H_2O), (D) IONPs@citrate@Eu (Fe : Eu = 1 : 1, in H_2O), and (F) IONPs@citrate@Eu (Fe : Eu = 1 : 0.25, in H_2O).

XPS scans confirm the presence of europium in the $Eu(OH)_3$ form for all Fe@Eu samples (Fig. 2(1)). The main ($3d_{5/2}$) peak is centered at 1135.6 eV for $Eu(OH)_3$ as reported previously.[76] The small peak that resolves at *ca.* 1127 eV can be attributed to Eu in the 2^+ oxidation state, indicative of defects on the surface.[67,77] For IONPs@citrate@Eu (Fe : Eu = 1 : 1, in H_2O and Fe : Eu = 1 : 3, in H_2O), the 3^+ oxidation state peaks show a slightly higher FWHM and a slightly different peak shape (see the $3d_{3/2}$ peak shape).

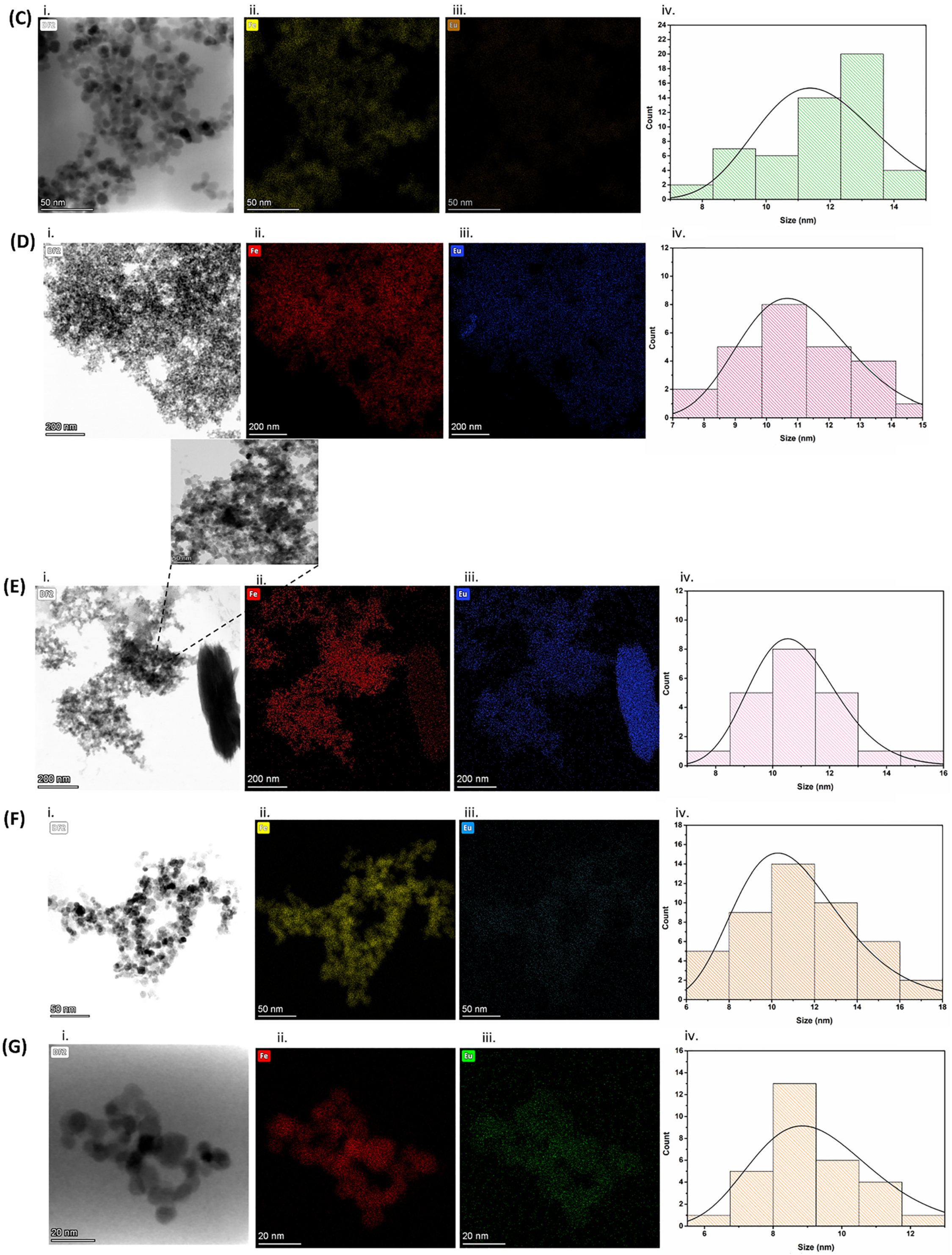

Fig. 3 TEM–EDX analyses of the Fe@Eu NPs. Size distribution was measured using ImageJ and analyzed using OriginPro 9.0. (C) IONPs@citrate@Eu (Fe : Eu = 1 : 3, in H_2O), (D) IONPs@citrate@Eu (Fe : Eu = 1 : 1, in H_2O), (E) IONPs@citrate@Eu (Fe : Eu = 1 : 1, in EG), (F) IONPs@citrate@Eu (Fe : Eu = 1 : 0.25, in H_2O), and (G) IONPs@citrate@Eu (Fe : Eu = 1 : 0.25, in EG).

These observations likely indicate the presence of a small amount of Eu_2O_3 in the sample, as the Eu^{+3} peaks for europium(III) oxide are slightly shifted to higher binding energies.[67] The spectrum maxima do not show a notable shift, and therefore the main component should be considered to be $Eu(OH)_3$. For IONPs@citrate@Eu (Fe : Eu = 1 : 0.25, in H_2O), the peaks shift to smaller binding energies, namely 1134.9 eV for the $3d_{5/2}$ component. Due to the low ratio of Eu/Fe in this sample, it is likely that the Eu–Fe interactions are stronger, reducing the binding energy of the peak.

The main Fe 2p photoelectron peak shows two main contributions centered at *ca.* 710 and 724 eV. Peak deconvolution is performed as reported by Atrei *et al.*[78] During deconvolution, identical constraints were applied to all spectra. The results reveal contributions from both Fe^2 and Fe^3 species, confirming the presence of magnetite (Fe_3O_4) in every sample. In Fig. 2(2), peaks assigned to Fe^2 are shown in red, while those assigned to Fe^3 are in green. The Fe^2 state is characterized by the $2p_{3/2}$ peak at 709.8 eV, a satellite at 716.4 eV, and the $2p_{1/2}$ peak at 723.0 eV. The Fe^3 state includes the 711.1 eV peak (octahedral sites), the 713.7 eV peak (tetrahedral sites), a satellite at 719.4 eV, and the $2p_{1/2}$ component at 724.9 eV. The Fe^3/Fe^2 ratio increases with higher Eu/Fe content, reaching 2.94 for IONPs@citrate@Eu (Fe : Eu = 1 : 3, H_2O), compared to 2.26 for the control IONPs@citrate. This corresponds to a total Fe valence of +8.1 in the magnetite structure, consistent with the expected value of +8.

The C 1s spectra (Fig. 2(3)) show contributions from four peaks. Adventitious carbon is set at 284.8 eV, with C–OH species appearing at 286.0 eV. C=O species are present at 287.6 eV and O–C=O contributions are centered at 288.8 eV.[79] Oxygenated species arise from the exposure of the sample to air and background gases present in the UHV system. The peak at *ca.* 294 eV is attributed to Eu and specifically the $4p_{1/2}$ bound state, indicating that the contribution from this peak weakens with decreasing Eu content in the sample.[80]

The O 1s region (Fig. 2(4)) deconvolutes into contributions from M–O_x (Fe_xO_y, Eu_xO_y) groups at 529.7 eV, –OH, M–OH species at *ca.* 531.5 eV from surface hydroxyl groups, and Eu–OH. For the Eu doped samples, this peak shows a slight shift to higher binding energies due to the contributions from the Eu–OH species. Another peak resolves at *ca.* 533.5 eV for surface impurities and carboxylate species present through sample preparation. Finally, for IONPs@citrate@Eu (Fe : Eu = 1 : 1, in H_2O), one more peak can be resolved in the region at 535.2 eV. Peaks at such binding energies could indicate the presence of water in the sample.[67,78,81]

TEM–EDX analysis. As shown in TEM images (Fig. 3), the samples consist of spherical-like Fe@Eu NPs with an average size of 9–12 nm and slight aggregation. At a 1 : 1 ratio, nanorods can be clearly observed, confirming the previous results. Mapping and elemental analysis were also performed for the samples. EDX spectra (Fig. S4 of the SI) demonstrated the existence of Fe, Eu, and O, confirming that europium is successfully incorporated in all samples. From the mapping, it can be validated that the nanorods mainly consist of Eu and O and only a small amount of Fe. In contrast, in the case of the nanospheres, there is a uniform distribution of Eu, Fe, and O. The ratio of Fe : Eu initially added for the syntheses is different from the obtained one. From Table 4, it can be observed that only a small amount of Eu can be incorporated in the magnetite structure, something that is probably attributed to the defects of the magnetite lattice and the larger radius of Eu. An important conclusion that can be drawn here is that the size of the Fe@Eu NPs is much smaller than the one measured with DLS.

PL spectroscopy. According to the literature, the compounds of Eu(III) and Eu(II) present characteristic photoluminescence, which is dependent on the media in which these elements are doped. In the case of Eu(III), whether this ion is doped into crystalline matrices or complexed with organic ligands, a very intense red photoluminescence is observed under UV irradiation. The obtained photoluminescence spectra of Eu(II) compounds give more information than the respective absorption spectra and result from the electron transitions from the $^5D_0$ excited state to the J levels (0–6) of the ^7F_J ground state in the wavelength range of 570–840 nm. Among the transitions, $^5D_0 \rightarrow {}^7F_2$ is the most intense and hypersensitive, giving the characteristic red photoluminescence of Eu(III) between 610 and 630 nm, whilst $^5D_0 \rightarrow {}^7F_5$ and $^5D_0 \rightarrow {}^7F_6$ are rarely observed depending on the detection wavelength limits of the spectrofluorimeters (*vide infra*).[20,82–84] Different from the trivalent europium, Eu(II) compounds under near-UV irradiation exhibit broad emission bands, which are due to the allowed electron transitions from the $4f^65d^1$ (E_g) lower excited state to the $4f^7$ ($^8S_{7/2}$) ground state.[85–87] These transitions are usually observed between 450 and 480 nm.[88] For example, Eu(II) doped in fluorides emits in the violet region of the visible light spectrum,

Table 4 Results of elemental analysis of EDX spectra

Sample	*Z*	Element	Mass fraction (%)	Obtained Fe : Eu	Size distribution (± SD) [nm]
IONPs@citrate@Eu (Fe : Eu = 1 : 3, in H_2O)	26	Fe	94.55	1 : 0.06	11.8 ± 1.8
	63	Eu	5.45		
IONPs@citrate@Eu (Fe : Eu = 1 : 1, in H_2O)	26	Fe	88.37	1 : 0.13	11.1 ± 1.8
	63	Eu	11.63		
IONPs@citrate@Eu (Fe : Eu = 1 : 1, in EG)	26	Fe	64.77	1 : 0.54	10.8 ± 1.6
	63	Eu	35.23		
IONPs@citrate@Eu (Fe : Eu = 1 : 0.25, in H_2O)	26	Fe	94.71	1 : 0.06	11.1 ± 2.5
	63	Eu	5.29		
IONPs@citrate@Eu (Fe : Eu = 1 : 0.25, in EG)	26	Fe	92.25	1 : 0.08	9.4 ± 2.0
	63	Eu	7.75		

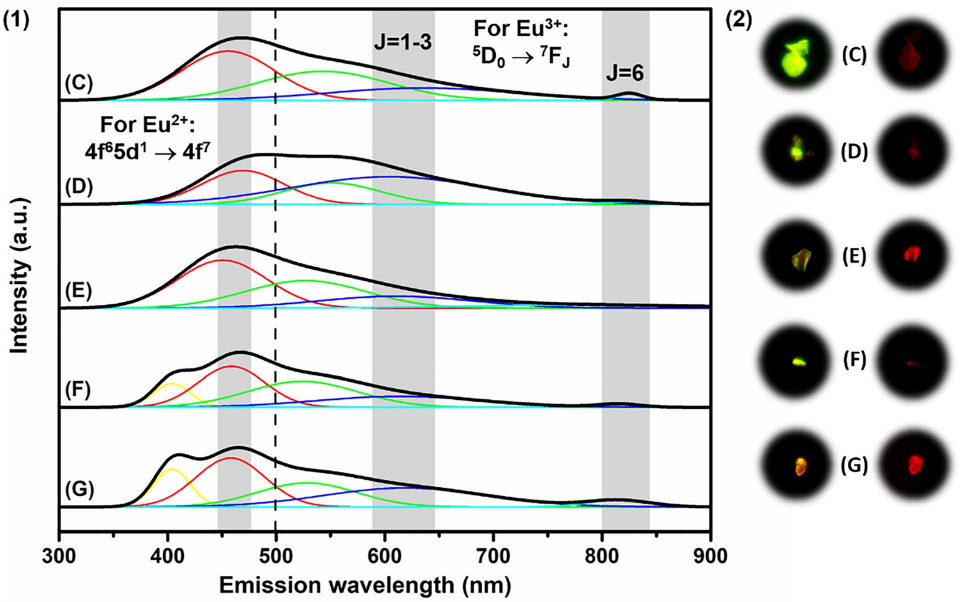

Fig. 4 (1) PL spectra of the Fe@Eu NPs at RT. The excitation wavelength is 350 nm. Peaks were smoothed using OriginPro 9.0. (2) Widefield optical fluorescence microscopy images of Fe@Eu NPs: (C) IONPs@citrate@Eu (Fe : Eu = 1 : 3, in H_2O), (D) IONPs@citrate@Eu (Fe : Eu = 1 : 1, in H_2O), (E) IONPs@citrate@Eu (Fe : Eu = 1 : 1, in EG), (F) IONPs@citrate@Eu (Fe : Eu = 1 : 0.25, in H_2O), and (G) IONPs@citrate@Eu (Fe : Eu = 1 : 0.25, in EG).

in chlorides and bromides the emission shifts to the violet/blue region, in oxides it occurs in the blue/green region, and in sulfides and thiocyanates it is shifted to the red region.[85]

From the PL spectra of the Fe@Eu NPs (Fig. 4(1)), two main clear peaks are detected after excitation at 350 nm. Specifically, a broad peak is observed around 470 nm, along with a weaker peak near 825 nm in the near-infrared (NIR) region. There is a high probability that the black core of magnetite absorbs a lot of the excitation light or there are a lot of formed defects on the host lattice, leading to a reduced emission intensity of europium.[89] This could explain the very broad peak centered around 470 nm, indicating green photoluminescence and, thus, the presence of Eu(II) in the Fe@Eu NPs, and overlapping the red photoluminescence of Eu(III) present in the precursor molecule. Gaussian fitting of each curve reveals that the broad main peak is composed of multiple underlying individual peaks. In more detail, the peak around 470 nm can be attributed to the $4f^65d^1 \rightarrow 4f^7$ transition of Eu(II) or it can be an indication that aggregates are formed, leading to Fe@Eu NPs of different sizes emitting light of higher energy. However, further analysis of this curve presents a broad peak between 590 and 650 nm attributed to the $^5D_0 \rightarrow {}^7F_{1-3}$ transitions of Eu(III). The peak of small intensity around 825 nm is attributed to the rarely observed $^5D_0 \rightarrow {}^7F_6$ transition of Eu(III).

Widefield optical fluorescence microscopy in Fe@Eu NPs. Additionally, europium, like other rare-earth elements, is known to undergo a "surface valence transition" phenomenon. In this process, variations in the surface geometry and coordination environment can lead to a prevalence of Eu(II) ions at the surface, while the bulk of the material retains Eu(III) or aliovalent states. This surface-bulk disparity further contributes to the observed dual-emission properties of the NPs.[90] As observed from the images in Fig. 4(2), a particularly interesting feature of the Fe@Eu NPs is their dual fluorescence behavior – exhibiting both green and red emissions. This suggests the simultaneous presence of Eu(II) and Eu(III) oxidation states within the structure. In some samples, red emission is more prominent, while in others, green emission dominates. Regardless of the emission color, the fluorescence intensity remains stable and persistent over time. A proposed mechanism for this dual emission involves the excitation of magnetite at a specific wavelength, where the absorbed energy is either sufficient to promote electrons from the valence band (VB) to the conduction band (CB), or becomes trapped in lattice defects. These trapped states may then facilitate non-radiative transitions to the discrete energy levels of Eu(III), resulting in characteristic luminescence.[91,92]

In vitro biological evaluation

Cell viability assay. The *in vitro* cytotoxicity studies were carried out using the MTT assay. This method is based on the reductive reaction of tetrazole of MTT to purple formazan in the mitochondria of living cells by reductase enzymes. The intensity of the purple color of formazan depicts the metabolic activity of the mitochondria and, thus, of the living cells.

The percentage of cell viability is determined by comparing the absorbance values of NP-treated cells to those of untreated controls. Subsequently, the cytotoxic potential of the NPs can be quantitatively evaluated through the construction of a dose–response curve, which illustrates the correlation between NP concentration and cell viability. NPs of very small size, around 10 nm, and their high positive charge improve penetration through the negatively charged bilipid membrane distributing iron molecules in the cells.[93] The levels of toxicity are correlated with surface modification, byproducts of the NPs, chemical composition of the different cell lines, oxidation state of IONPs

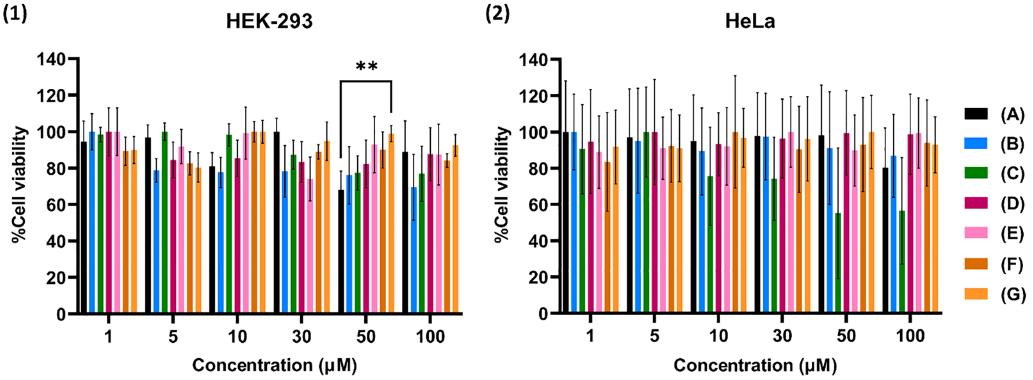

Fig. 5 MTT cytotoxicity assay of (1) HEK-293 and (2) HeLa cell lines. Cells were treated with 1, 5, 10, 30, 50 and 100 μM_{Fe} for 24 h. The calculation of the percentages was conducted using eqn (1), including the control, and values represent the mean value ± SD of three different triplicate experiments. The interaction is considered very significant for $^{**}p \leq 0.01$ (multiple comparisons were performed between the different NPs in the mean value of each concentration). NPs: (A) IONPs, (B) IONPs@citrate, (C) IONPs@citrate@Eu (Fe : Eu = 1 : 3, in H_2O), (D) IONPs@citrate@Eu (Fe : Eu = 1 : 1, in H_2O), (E) IONPs@citrate@Eu (Fe : Eu = 1 : 1, in EG), (F) IONPs@citrate@Eu (Fe : Eu = 1 : 0.25, in H_2O), and (G) IONPs@citrate@Eu (Fe : Eu = 1 : 0.25, in EG).

as well as the interaction between IONPs and proteins.[94] In general, administration of IONPs has been related to extensive cytotoxicity leading, for instance, to apoptosis, mitochondrial disorder, DNA damage, and excessive ROS production.[94,95] Nevertheless, coating of NPs with an amphiphilic layer enhances colloidal stability and improves their biodistribution, preventing agglomeration caused by intramolecular interactions or interactions with biological molecules and prolonging their circulation time.[94,96] Overall, the highest administered concentration of NPs is expected to be more toxic because of the metabolic differences.

Results in Fig. 5(1) demonstrate that, in most cases, cytotoxicity is dose-dependent in HEK-293 cells reaching 70% even after incubation with 100 μM_{Fe} for 24 h. In particular, IONPs@citrate, which is the precursor sample for the following syntheses, present viability around 70% or higher, whilst the same tendency is also observed in bare NPs. As for Fe@Eu NPs (C)–(G), viability seems to exceed 80%, indicating not only that these NPs are biocompatible with the specific cell line, but also that the addition of Eu leads to higher percentages of viability. HEK-293 is a cell line of human origin and, thus, the biocompatibility of the NPs is a positive first step for their application as a theranostic agent. From Fig. 5(2), without reference to dose-dependency, it can be observed that viability exceeds 70% in most cases underlying the biocompatibility of NPs with HeLa cells as well. However, a major change is observed after the administration of (*C*), which presents dose-dependent toxicity and leads to viability approximately equal to 50% after incubation with 100 μM_{Fe}. The size of all NPs is around 10 nm and their surface charge is positive, meaning that all of them can be easily internalized in cells. However, in HeLa cells probably the integrity of (*C*) is diminished, leading to high levels of available free iron molecules in the cells and increased toxicity.

Wound healing assay. The wound healing assay is one of the common methods used to study cell migration *in vitro*. Although this method is not an exact copy of cell migration *in vivo*, but a mimic of this process, its key feature is the monitoring of cell migration within a "wound", which has been created in a monolayer of cells.[97] The cells, located at the edges of the cell-free area, begin to move into it until the damaged cell–cell interactions are recreated and the "wound" is healed. The rate at which the space closes is a measure of the speed of the cell movement and proliferation altogether.[98]

This experiment was conducted for further determination of cytotoxicity, investigating the proliferation and migration of the cells through the scratched area. As can be observed from Fig. 6, there is a significant difference between the two cell lines with HEK-293 being more affected by the administration of the Fe@Eu NPs. In particular, comparing the images in Fig. 6(1) from (C) to (G) with the control, it can be concluded that cell proliferation is reduced, since 72 h after administering NPs a certain percentage of the wound is still open. However, more than 70% of the wound is healed in all cases. As for HeLa cells (Fig. 6(2)), proliferation does not appear to be very disturbed taking into consideration that the wound has reached almost 100% closure after 28 h of incubation. The only differences appear in cases (C) and (E), where healing slows down, leading to reduced proliferation.

Prussian blue staining and optical microscopy. This assay was applied to both HEK-293 and HeLa cells to assess NP uptake and internalization. The method specifically targets non-heme iron in its ionized form.[99] As shown in Fig. 7, cell nuclei are stained with nuclear fast red, while the presence of the blue complex indicates the localization of NP-derived iron within the cells. Results confirmed that the synthesized NPs were efficiently internalized in both cell lines after 24 hours of incubation, accumulating in the cytoplasm and around the nuclear membrane. As already mentioned, the internalization of NPs was attributed to citrate molecules, which contributed to the avoidance of agglomeration and the positive surface charge.

Fluorescence microscopy in cells. From the images of Fig. 8, it is apparent that the Fe@Eu NPs have been successfully internalized in the cells after 24 hours of incubation. The fluorescence of the cells is enhanced and, especially, in HeLa cells, which exhibit more intense fluorescence in contrast to HEK-293. This fluorescence is clearly attributed to the presence

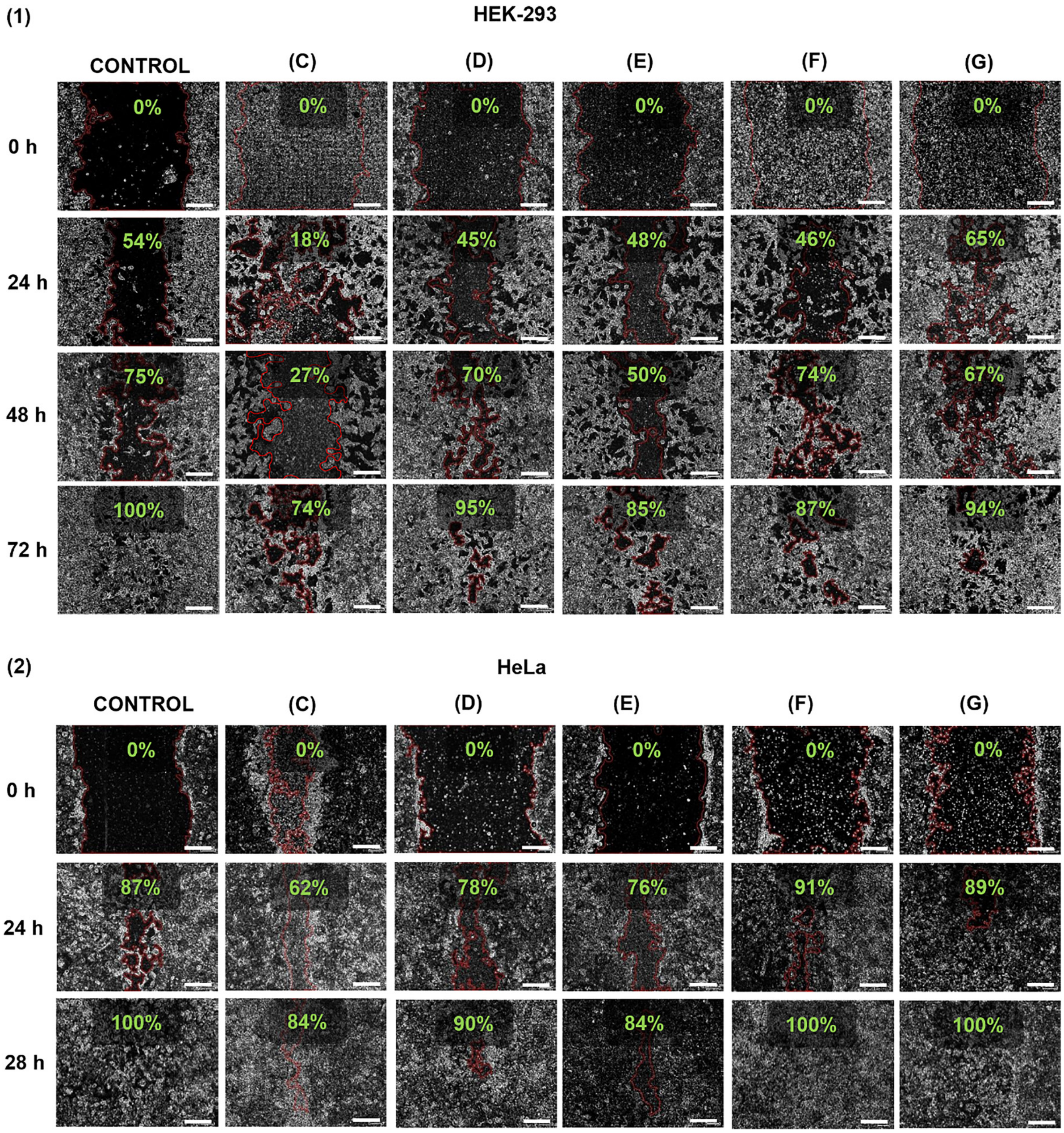

Fig. 6 Representative images of the wound healing assay of (1) HEK-293 and (2) HeLa cells after administration of 100 μM_{Fe} Fe@Eu NPs for 24 h. The calculation of the %wound closure was conducted using eqn (2). Scale bar: 0.1 mm. NPs: (C) IONPs@citrate@Eu (Fe : Eu = 1 : 3, in H_2O), (D) IONPs@citrate@Eu (Fe : Eu = 1 : 1, in H_2O), (E) IONPs@citrate@Eu (Fe : Eu = 1 : 1, in EG), (F) IONPs@citrate@Eu (Fe : Eu = 1 : 0.25, in H_2O), and (G) IONPs@citrate@Eu (Fe : Eu = 1 : 0.25, in EG).

of europium in NPs, since there is no indication of self-fluorescence of the cells in the control group. At this point, it is worth noting that the cells of most organisms show some levels of autofluorescence, which are due to the presence of metabolites and structural components, such as nicotinamide adenine dinucleotide phosphate (NAD(P)H), proteins containing aromatic amino acids, and riboflavins.[100] The natural light emission of these molecules increases, especially when there is enhanced cellular metabolism, thereby interfering with the light emission of other components administered to the cells.[101] Enhanced cell metabolism is mainly observed when cells are stressed and trying to maintain their homeostasis.[102] According to this, it is possible that the enhanced fluorescence of HeLa is attributed not only to the presence of the Fe@Eu NPs, but also to the increased stress they are under, as opposed to HEK-293. These images lead to the conclusion that the specific NPs are good candidates for bioimaging use.

Effect on cell cycle distribution. To assess whether Fe@Eu NPs influence cell cycle regulation, we conducted flow cytometry analysis to investigate apoptosis-induced cell death and cell cycle distribution.

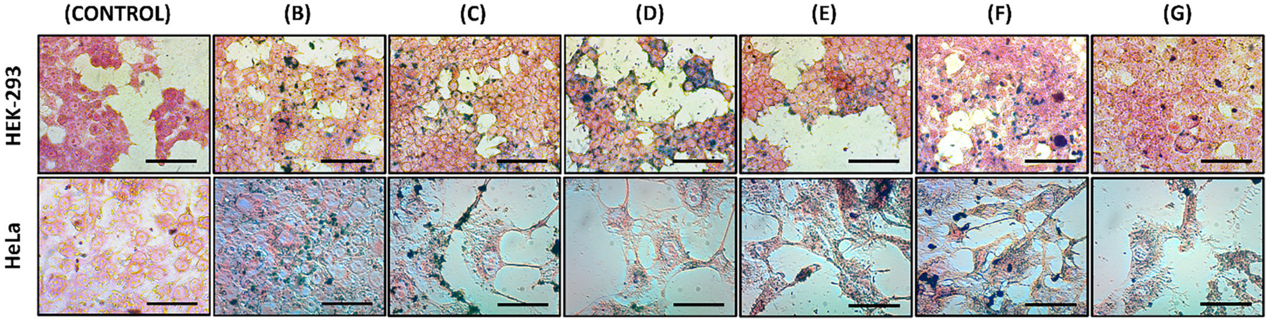

Fig. 7 Optical microscopy images after cells were treated with 100 μM_{Fe} NPs for 24 h and stained with Prussian blue. Scale bar: 0.1 mm. NPs: (B) IONPs@citrate, (C) IONPs@citrate@Eu (Fe : Eu = 1 : 3, in H_2O), (D) IONPs@citrate@Eu (Fe : Eu = 1 : 1, in H_2O), (E) IONPs@citrate@Eu (Fe : Eu = 1 : 1, in EG), (F) IONPs@citrate@Eu (Fe : Eu = 1 : 0.25, in H_2O), and (G) IONPs@citrate@Eu (Fe : Eu = 1 : 0.25, in EG).

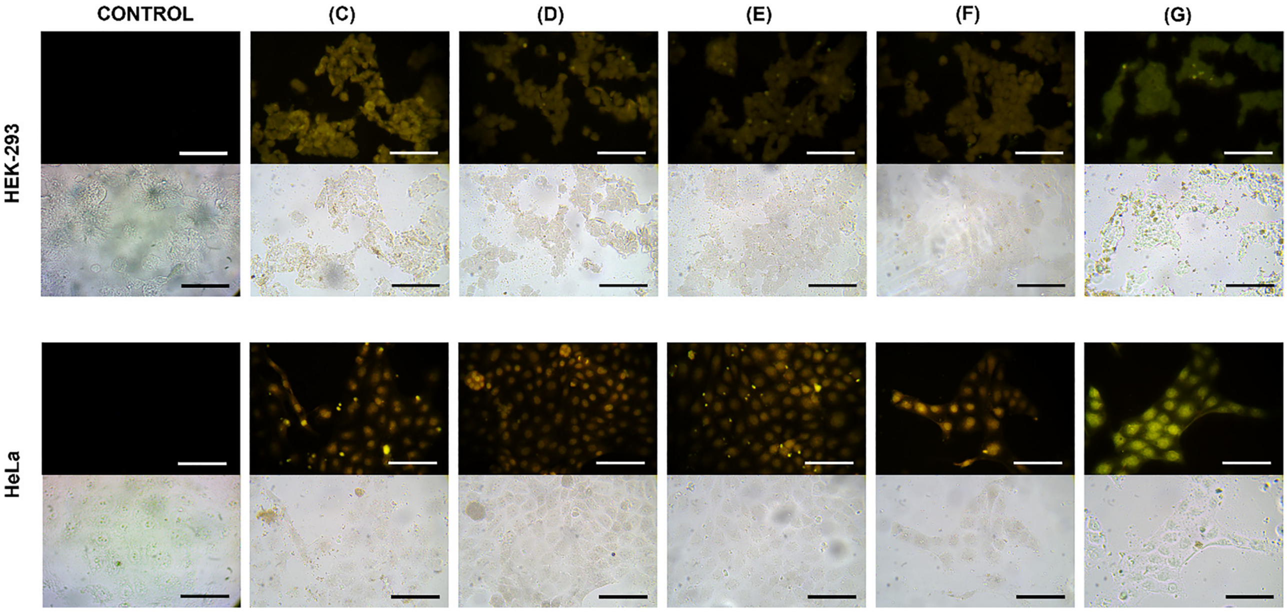

Fig. 8 Fluorescence microscopy images of HEK-293 and HeLa after treatment with 100 μM_{Fe} Fe@Eu NPs for 24 h. For each sample, there is a match of images from optical microscopy and fluorescence microscopy. Images were taken after blue laser irradiation (excitation 410–490 nm, emission: 515 nm). Scale bar: 0.1 mm. NPs: (C) IONPs@citrate@Eu (Fe : Eu = 1 : 3, in H_2O), (D) IONPs@citrate@Eu (Fe : Eu = 1 : 1, in H_2O), (E) IONPs@citrate@Eu (Fe : Eu = 1 : 1, in EG), (F) IONPs@citrate@Eu (Fe : Eu = 1 : 0.25, in H_2O), and (G) IONPs@citrate@Eu (Fe : Eu = 1 : 0.25, in EG).

HEK-293 and HeLa cells were treated with Fe@Eu NPs at a concentration of 100 μM_{Fe} for 24 h. This concentration was selected based on prior MTT assay results, which confirmed that the NPs maintain biocompatibility at this dose. The DNA content in the various phases of the cell cycle was then analyzed to determine any perturbations caused by NP exposure. As a positive control, DNR was employed, a chemotherapeutic agent well known for its potent cytostatic and cytotoxic effects. DNR intercalates into DNA, generates reactive oxygen species (ROS), inhibits topoisomerase II activity, and forms DNA adducts, all of which contribute to structural and functional damage to DNA and the cell membrane.[103,104] In response to this damage, cells typically undergo cell cycle arrest, providing time for DNA repair mechanisms to be activated. This experimental setup enables the comparison of Fe@Eu NP-induced effects to those of a well-established cytotoxic agent.

From the results in Fig. 9, it can be stated that cell cycle distribution presents differences in both cell lines, HEK-293 and HeLa, in a divergent way after the administration of Fe@Eu NPs. In particular, observing the control group in Fig. 9(1) and Fig. S5(1), a normal cell cycle in HEK-293 consists of an increased population in G1 and S phases, while it decreases to half in G2 and post-G2 phases and is almost nil in the sub-G1 phase. As for HeLa cells, observing the control group in Fig. 9(2) and Fig. S5(2), a normal cell cycle consists of an almost evenly distributed population in G1, S and G2 phases, whilst it reaches almost zero point in the sub-G1 phase and evolves in the post-G2 phase. Cytostatic DNR affects the cell cycle of HEK-293 by extremely increasing the DNA content in the sub-G1 phase, meaning that a large percentage of cells is driven to apoptosis before they even enter the cell cycle.[105,106] As a result, the distribution of cells in the other phases is reduced, especially

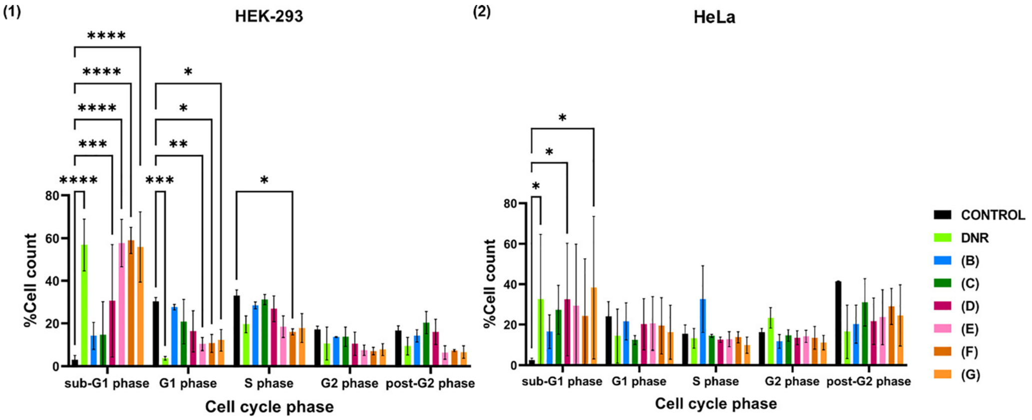

Fig. 9 Plot of the percentage of cell content in the sub-G1, G1, S, G2, and post-G2 phases of (3) HEK-293 and (4) HeLa cells after treatment with NPs of 100 μM_{Fe} for 24 h. Data are represented as mean value ± SD (three independent experiments). The interaction is considered statistically significant for $^*p \leq 0.05$, very significant for $^{**}p \leq 0.01$, highly significant for $^{***}p \leq 0.001$ and extremely significant for $^{****}p \leq 0.0001$ (multiple comparisons were performed between the different NPs in the mean value of each phase). NPs: (B) IONPs@citrate, (C) IONPs@citrate@Eu (Fe : Eu = 1 : 3, in H_2O), (D) IONPs@citrate@Eu (Fe : Eu = 1 : 1, in H_2O), (E) IONPs@citrate@Eu (Fe : Eu = 1 : 1, in EG), (F) IONPs@citrate@Eu (Fe : Eu = 1 : 0.25, in H_2O), and (G) IONPs@citrate@Eu (Fe : Eu = 1 : 0.25, in EG).

in the G1 phase. As for HeLa cells, cell cycle distribution follows a different pathway after the administration of DNR with DNA content being increased in sub-G1 and G2 phases.

Comparing the results of the negative and positive controls with those of the administered Fe@Eu NPs, some interesting results were observed. In particular, administration of (B) to HEK-293 leads to cell cycle distribution similar to that of the negative control, meaning that the cell cycle is not disturbed. This is probably attributed to the surface modification of IONPs, which contributes to avoidance of agglomeration and release of iron ions in the cell. The same tendency is also observed after administering (C). Nevertheless, this pattern ceases to be valid for NPs (D)–(G), for which the sub-G1 phase increases dramatically and the population in the next phases is diminished, as observed in DNR. Since (D) and (E) are colloidally stable, cell cycle distribution could be correlated with the presence of rods in the sample or the release of increased iron ions. For (F) and (G), agglomeration of Fe@Eu NPs is an extra reason for the disturbance of the cell cycle. As for HeLa cells, it seems that administration of all NPs results in increased DNA content in sub-G1 and post-G2 phases, meaning that a large percentage of cells is driven to apoptosis at the beginning and the end of the cycle. Only a small percentage of cells remain unaffected, continuing the cell cycle under normal conditions. According to the literature, increased reactive oxygen species (ROS) generation has been previously associated with elevated levels of apoptosis in cancer cells. Substances leading to increased levels of ROS and apoptosis are considered good candidates for anticancer agents and, thus, cancer therapy.[107]

Production of intracellular ROS. The increased percentages of toxicity acquired after the administration of the NPs have been previously attributed to the pervasive ROS production promoting extensive oxidative stress. There is a hypothesis that IONPs, after uptake and internalization in the cells, undergo enzymatic degradation by lysosomes' acidic environment releasing Fe(II). These ions react with hydrogen peroxide produced in mitochondria generating highly reactive hydroxyl radicals and Fe(III) through the Fenton reaction. Excessive production of ROS leads to the inflammation of cells, affecting mitochondrial functionality and releasing cytochrome *c*, which adjusts membrane potential, directly damages DNA, proteins and lipids, and causes apoptosis. The presence of ROS reduces the defense capability of physical antioxidants inside cells resulting in oxidative stress.[108,109] Oxidative stress is a process that causes severe cytotoxicity and even cell death.[110] In addition, the NPs' crystallinity, size, and agglomeration level can also be associated with their increased ROS production even after short-term treatment.[52,111] ROS and H_2O_2 are the main species found endogenously in cells, but the levels in cancer cells are much higher than in healthy cells. They typically help with maintaining homeostasis and cell signaling. The reaction between the endogenous H_2O_2 and IONPs produces hydroxyl radicals and, thus, presents peroxidase-like activity. However, to kill the cells, usually the addition of extra H_2O_2 is needed.[112]

By analyzing the results in Fig. 10 (and Fig. S6 of the SI), it can be confirmed that IONPs induce the generation of ROS in both cell lines. According to the literature, both cell lines internalize NPs *via* endocytosis, but the magnitude of ROS induction can differ due to variations in metabolic activity, iron handling capacity, and baseline antioxidant defense between the two cell types. In particular, HeLa cells are reported to upregulate antioxidant mechanisms at earlier time points, which may transiently mitigate oxidative stress but become insufficient upon prolonged exposure (24 h), resulting in elevated ROS levels. Conversely, HEK-293 cells, while showing a more acute ROS response initially, appear to possess more effective early cytoprotective responses that stabilize ROS levels over time.[113] In the present study, treatment of HEK-293 cells with NPs of 100 μM_{Fe} results in lower ROS levels compared to HeLa cells under the same conditions. Notably, after administration of formulation (B), ROS levels increased by approximately 50% beyond the baseline in HEK-293 cells, whereas the increase in HeLa cells

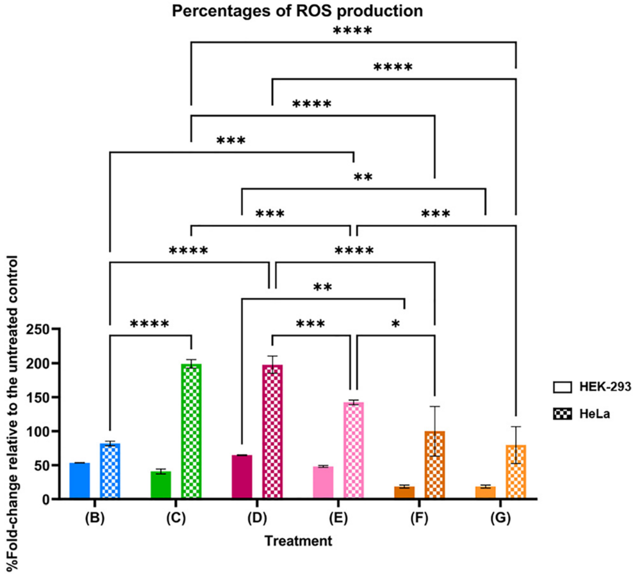

Fig. 10 Plot of the percentages of the produced ROS in HEK-293 and HeLa cells relative to the untreated control after treatment with NPs of 100 μM_{Fe} for 24 h. Data are represented as mean value ± SD (three independent experiments). The interaction is considered statistically significant for $*p \leq 0.05$, very significant for $**p \leq 0.01$, highly significant for $***p \leq 0.001$, and extremely significant for $****p \leq 0.0001$ (multiple comparisons were performed between the different NPs in the mean value for each cell line). NPs: (B) IONPs@citrate, (C) IONPs@citrate@Eu (Fe : Eu = 1 : 3, in H_2O), (D) IONPs@citrate@Eu (Fe : Eu = 1 : 1, in H_2O), (E) IONPs@citrate@Eu (Fe : Eu = 1 : 1, in EG), (F) IONPs@citrate@Eu (Fe : Eu = 1 : 0.25, in H_2O), and (G) IONPs@citrate@Eu (Fe : Eu = 1 : 0.25, in EG).

was around 80%. This suggests that the presence of intracellular IONPs – along with moderate particle dissolution and subsequent iron ion release – may more strongly impact the redox balance in HeLa cells. The same trend appears with increasing europium content, indicating a formulation-dependent modulation of oxidative stress. Of particular interest are formulations (C) and (D), which cause significant ROS elevation, especially in HeLa cells. This effect may be attributed to differences in NP size, morphology, rate of intracellular ion release, or the interaction with cellular antioxidant systems and can support the selective pro-oxidant and pro-apoptotic effects of these formulations. In the case of formulation (C), it can also be observed that administration to HEK-293 does not elevate the ROS percentage significantly reinforcing their biosafety. The consistently higher ROS levels observed in HeLa cells can also be explained by their transformed phenotype. As a cancer-derived cell line, HeLa cells typically exhibit elevated metabolic rates and mitochondrial activity, rendering them more vulnerable to oxidative stress. This vulnerability is further exacerbated by their NP accumulation intracellularly, resulting in enhanced ROS generation. Formulations (E), (F), and (G) also increase the levels of ROS, without this elevation being very significant biologically. The possibility of ROS elevation being responsible for the apoptosis and the disturbance of the cell cycle is extremely high, given that apoptosis and ROS production have been previously correlated with the presence of iron and interference with the Fenton reaction.

Apoptotic and necrotic pathways. The evaluation and measurement of the population of viable, apoptotic (early and late) and necrotic cells were conducted after the treatment of HEK-293 and HeLa cells with NPs of 100 μM_{Fe} for 24 h. The specific time point was selected in order to corroborate the MTT results and examine the eventuality of induction of apoptosis in the presence of the NPs, as indicated by the cell cycle.

As shown in Fig. 11 (and Fig. S7 in the SI), treatment with the NPs induces high levels of apoptosis in both cell lines. In particular, the percentage of total apoptotic HEK-293 cells ranges between 40 and 70%, with most of the population in

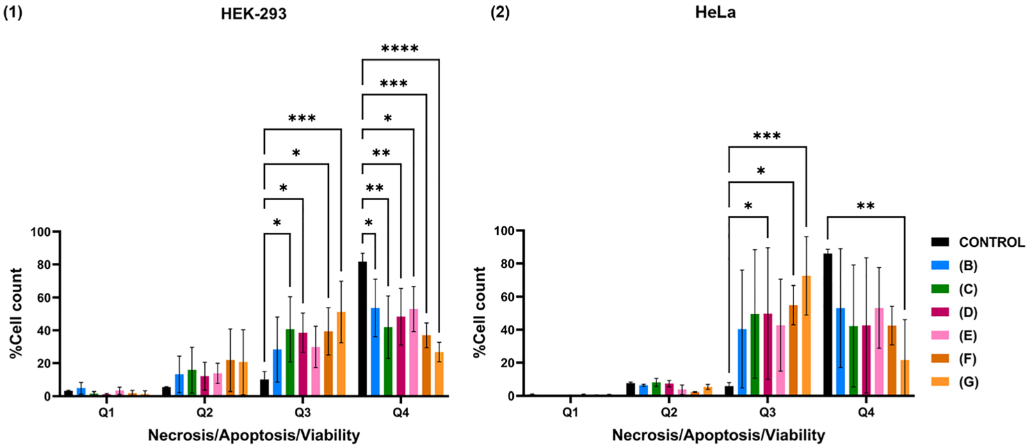

Fig. 11 Plot of the percentage of cell content in Q1, Q2, Q3, and Q4 gates in (3) HEK-293 and (4) HeLa cells after treatment with NPs of 100 μM_{Fe} for 24 h. Data are represented as mean value ± SD (three independent experiments). The interaction is considered statistically significant for $*p \leq 0.05$, very significant for $**p \leq 0.01$, highly significant for $***p \leq 0.001$, and extremely significant for $****p \leq 0.0001$ (multiple comparisons were performed between the different NPs in the mean value of each phase). NPs: (B) IONPs@citrate, (C) IONPs@citrate@Eu (Fe : Eu = 1 : 3, in H_2O), (D) IONPs@citrate@Eu (Fe : Eu = 1 : 1, in H_2O), (E) IONPs@citrate@Eu (Fe : Eu = 1 : 1, in EG), (F) IONPs@citrate@Eu (Fe : Eu = 1 : 0.25, in H_2O), and (G) IONPs@citrate@Eu (Fe : Eu = 1 : 0.25, in EG).

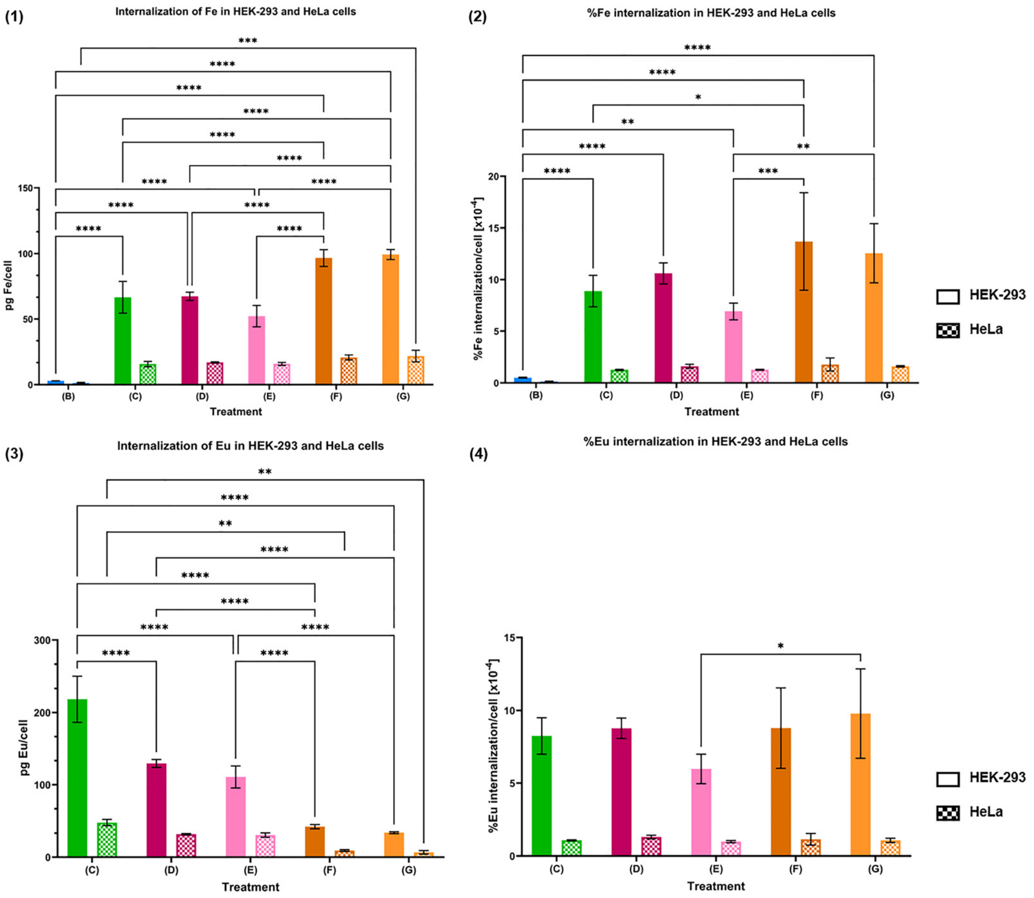

Fig. 12 Plots of the concentration of (1) Fe (pg Fe/cell) and (3) Eu (pg Eu/cell), as well as the respective percentages of (2) Fe (%Fe/cell) and (4) Eu (%Eu/cell) internalized in HEK-293 and HeLa cells after treatment with NPs of 100 μM_{Fe} for 24 h. Data are represented as mean value ± SD (three independent experiments). The interaction is considered statistically significant for $^{*}p \leq 0.05$, very significant for $^{**}p \leq 0.01$, highly significant for $^{***}p \leq 0.001$, and extremely significant for $^{****}p \leq 0.0001$ (multiple comparisons were performed between the different NPs in the mean value for each cell line). NPs: (B) IONPs@citrate, (C) IONPs@citrate@Eu (Fe : Eu = 1 : 3, in H_2O), (D) IONPs@citrate@Eu (Fe : Eu = 1 : 1, in H_2O), (E) IONPs@citrate@Eu (Fe : Eu = 1 : 1, in EG), (F) IONPs@citrate@Eu (Fe : Eu = 1 : 0.25, in H_2O), and (G) IONPs@citrate@Eu (Fe : Eu = 1 : 0.25, in EG).

early apoptosis. A similar pattern is observed in HeLa cells, with total apoptotic cells ranging from 45% to 75%, and the majority of population concurrently entering early apoptosis. The percentage of necrotic cells may be negligible in both cell lines; however, the present experiment confirms that the apoptotic pathway is the one followed and leads the cells to cell death after 24 h of incubation. As already stated in the literature and confirmed by our study, the presence of iron inside the cells contributes to the elevation of ROS due to the Fenton reaction and, as a consequence, cells are driven to apoptosis.

Intracellular iron and europium quantification *via* ICP-MS. To support the above findings and further comprehend the mechanism of action of the NPs, the intracellular levels of Fe and Eu in HEK-293 and HeLa cells were quantified using ICP-MS. As shown in Fig. 12, both elements exhibit greater accumulation in HEK-293 cells compared to HeLa cells. Specifically, treatment with formulation (B) resulted in the lowest Fe uptake in both cell lines. This effect can be attributed to the negative surface charge of the NPs, which may repel the negatively charged cell membrane, thereby hindering their entry into the intracellular environment. In contrast, formulations (C) to (G), which possess positively charged surfaces, exhibited enhanced cellular internalization—likely facilitated by electrostatic attraction between the NPs and the cell membrane.

Overall, HEK-293 cells appear to internalize Fe@Eu NPs more efficiently than HeLa cells, as indicated by the consistently higher intracellular concentrations of both Fe (Fig. 12 (1) and (2)) and Eu (Fig. 12 (3) and (4)). Notably, the accumulation of Fe and Eu in HeLa cells reaches only about one-fourth to one-third of the levels observed in HEK-293 cells.

Considering the combined findings, including ICP-MS data, several important conclusions can be drawn regarding the behavior of the synthesized Fe@Eu NPs in healthy *versus* cancerous cell lines. Specifically, treatment with 100 μM_{Fe} of NPs resulted in more efficient internalization in HEK-293 cells, accompanied by only moderate cytotoxicity. In contrast, despite lower internalization levels in HeLa cells, the NPs triggered more pronounced biological responses. These included a significant reduction in cell viability, enhanced *in vitro* fluorescence, elevated ROS production, and increased apoptosis after 24 hours of exposure.

These observations suggest that, although fewer NPs accumulate in HeLa cells, the internalized concentrations of Fe and

Eu are sufficient to disrupt key metabolic pathways and induce substantial oxidative stress. The elevated oxidative stress levels may also underlie the enhanced fluorescence observed in HeLa cells following NP treatment.

Conclusions

In summary, this work presents the synthesis of optomagnetic Fe@Eu NPs composed of iron and europium at varying Fe : Eu molar ratios (1 : 3, 1 : 1, and 1 : 0.25), following a rapid, straightforward, and environmentally friendly co-precipitation method. Surface modification of the IONPs with citrate improved colloidal stability, though the introduction of europium at different amounts induced slight aggregation. Morphologically, the NPs were predominantly spherical-like, with an average diameter of approximately 10 nm; however, nanorod formation was observed at higher europium content. Structural characterization confirmed that europium was incorporated into the magnetite crystal structure or deposited on the particle surface. A particularly notable property of these NPs is their dual fluorescence capability under UV irradiation, enhancing their potential as multimodal imaging agents.

Biological evaluation demonstrated the overall biocompatibility of the Fe@Eu NPs in both healthy (HEK-293) and cancerous (HeLa) cell lines following 24-hour treatment. After cellular uptake, the NPs were found to interfere with the Fenton reaction, resulting in ROS generation, apoptosis induction, and mild disruption of the cell cycle. The magnitude of these effects varied with the Fe : Eu ratio, suggesting that the biological activity of the NPs can be tuned by adjusting their composition. This tunability supports their versatility across different biomedical applications.

Comparative analysis between HEK-293 and HeLa cells provided valuable insights into cellular responses and therapeutic relevance. In HEK-293 cells, formulations (B) and (C) caused minimal disruption to the cell cycle, closely resembling the untreated control. This suggests that the surface-modified IONPs effectively limited intracellular iron release and prevented excessive oxidative stress, maintaining cellular homeostasis in healthy tissues. In contrast, formulations (D) through (G) induced significant cell cycle arrest at the sub-G1 phase – a marker of apoptosis – along with a reduction in cells progressing through subsequent phases. These effects are likely due to increased iron ion release, agglomeration, or the presence of anisotropic (rod-like) structures.

In HeLa cells, all nanoparticle variants led to notable increases in sub-G1 and post-G2 DNA contents, indicating robust apoptotic activity. These findings are consistent with previous reports linking high intracellular ROS levels to apoptosis in cancer cells. ROS assays further supported this, revealing statistically significant ROS increases in HeLa cells, particularly in response to formulations (C) and (D). These effects are attributed to the enhanced oxidative potential introduced by europium incorporation, which may modulate surface chemistry and iron ion dynamics.

Further analysis of NPs' interference in various pathways of programmed cell death was conducted utilizing flow cytometry. It was confirmed that substantial levels of early apoptosis across both cell lines were produced, with minimal necrosis observed. Apoptosis levels ranged from 40 to 70% in HEK-293 and 45–75% in HeLa cells, confirming that apoptosis is the primary mode of cell death, likely driven by intracellular iron-mediated ROS production.

Importantly, formulation (C) emerged as the most selective and promising candidate, demonstrating minimal cytotoxicity toward healthy HEK-293 cells while inducing significant apoptotic activity in HeLa cancer cells. This dual selectivity highlights a potential therapeutic window, making formulation (C) especially attractive for targeted cancer therapy with reduced risk to surrounding healthy tissue. Collectively, these findings underscore the multifunctional nature of Fe@Eu NPs: strong fluorescence emission suitable for imaging combined with selective induction of apoptosis in cancer cells. Their favorable biocompatibility in non-cancerous cells, alongside their capacity to selectively induce oxidative stress in cancerous environments, position these nanostructures as promising candidates for further development in cancer diagnostics and therapeutics.

Author contributions

Evangelia Tsitsou: data curation, formal analysis, investigation, visualization, writing – original draft. Danai Prokopiou: investigation. Athina Papadopoulou: investigation. Alexandros K. Bikogiannakis: investigation, formal analysis. Georgios Kyriakou: investigation, resources. Elias Sakellis: investigation. Nikos Boukos: resources. Marios Kostakis: investigation, Nikolaos S. Thomaidis: resources. Eleni K. Efthimiadou: project administration, funding acquisition, conceptualization, supervision, resources, methodology, writing – review & editing.

Conflicts of interest

There are no conflicts to declare.

Data availability

The data supporting this manuscript are available from the author upon request.

Supplementary information is available. See DOI: **https://doi.org/10.1039/d5ma00659g**.

Acknowledgements

This work was conducted with the financial support through the Special Account for Research Grants (S. A. R. G.) from the National and Kapodistrian University of Athens (N. K. U. A.). All powder diffraction data were collected at the National and Kapodistrian University of Athens X-Ray Diffraction Core Facility. The creation of the graphical abstract was carried out using the BioRender.com platform, ChemDraw Ultra 12.0 program, and Microsoft PowerPoint.

References

1 N. Baig, I. Kammakakam and W. Falath, *Mater. Adv.*, 2021, **2**, 1821–1871.

2 B. Fu, J. Sun, Y. Cheng, H. Ouyang, G. Compagnini, P. Yin, S. Wei, S. Li, D. Li, V. Scardaci and H. Zhang, *Adv. Funct. Mater.*, 2021, **31**, 2107363.

3 L. A. Kolahalam, I. V. Kasi Viswanath, B. S. Diwakar, B. Govindh, V. Reddy and Y. L. N. Murthy, *Mater. Today Proc.*, 2019, **18**, 2182–2190.

4 J. Silver, in *Chemistry of Iron*, ed. J. Silver, Springer, Netherlands, Dordrecht, 1993, pp. 1–29.

5 D. Nicholls, *Comprehensive Inorganic Chemistry*, Pergamon Press, Exeter, 1973, vol. 24.

6 A. S. Teja and P.-Y. Koh, *Prog. Cryst. Growth Charact. Mater.*, 2009, **55**, 22–45.

7 N. Ajinkya, X. Yu, P. Kaithal, H. Luo, P. Somani and S. Ramakrishna, *Materials*, 2020, **13**, 4644.

8 M. Wegmann and M. Scharr, *Precision Medicine*, Elsevier, 2018, pp. 145–181.

9 M. G. Montiel Schneider, M. J. Martín, J. Otarola, E. Vakarelska, V. Simeonov, V. Lassalle and M. Nedyalkova, *Pharmaceutics*, 2022, **14**, 204.

10 A. V. Samrot, C. S. Sahithya, J. Selvarani A, S. K. Purayil and P. Ponnaiah, *Curr. Res. Green Sustainable Chem.*, 2021, **4**, 100042.

11 M. R. Ghazanfari, M. Kashefi, S. F. Shams and M. R. Jaafari, *Biochem. Res. Int.*, 2016, **2016**, 1–32.

12 G. S. Demirer, A. C. Okur and S. Kizilel, *J. Mater. Chem. B*, 2015, **3**, 7831–7849.

13 M. Bustamante-Torres, D. Romero-Fierro, J. Estrella-Nuñez, B. Arcentales-Vera, E. Chichande-Proaño and E. Bucio, *Polymers*, 2022, **14**, 752.

14 A. K. Sharma, *Nanotheranostics*, 2023, **7**, 258–269.

15 A. Zaleska-Medynska, M. Marchelek, M. Diak and E. Grabowska, *Adv. Colloid Interface Sci.*, 2016, **229**, 80–107.

16 K. Loza, M. Heggen and M. Epple, *Adv. Funct. Mater.*, 2020, **30**, 1909260.

17 R. Pujales-Paradela, T. Granath, M. T. Seuffert, T. Kasper, K. Müller-Buschbaum and K. Mandel, *J. Mater. Chem. C*, 2022, **10**, 1017–1028.

18 M. Runowski, T. Grzyb and S. Lis, *J. Nanopart. Res.*, 2012, **14**, 1188.

19 C. Wang, L. Xu, X. Li and Q. Lin, *Chem. Phys. Chem.*, 2012, **13**, 3765–3772.

20 S. S. Syamchand and G. Sony, *J. Lumin.*, 2015, **165**, 190–215.

21 J. Qin, G. Liang, Y. Feng, B. Feng, G. Wang, N. Wu, Y. Zhao and J. Wei, *Nanoscale*, 2020, **12**, 6096–6103.

22 Z. Li, Y. Zhang, B. Shuter and N. Muhammad Idris, *Langmuir*, 2009, **25**, 12015–12018.

23 R. R. Silva, A. P. Duarte, R. M. Sábio, J. M. A. Caiut, M. Gressier, M.-J. Menu, A. Franco and S. J. L. Ribeiro, *ChemistrySelect*, 2016, **1**, 5923–5928.

24 C. R. De Silva, S. Smith, I. Shim, J. Pyun, T. Gutu, J. Jiao and Z. Zheng, *J. Am. Chem. Soc.*, 2009, **131**, 6336–6337.

25 S. Han, Y. Tang, H. Guo, S. Qin and J. Wu, *Nanoscale Res. Lett.*, 2016, **11**, 273.

26 S. Chakraborty, K. S. Sharma, A. Rajeswari, K. V. Vimalnath, H. D. Sarma, U. Pandey, J. Jagannath, R. S. Ningthoujam, R. K. Vatsa and A. Dash, *J. Mater. Chem. B*, 2015, **3**, 5455–5466.

27 L. Yang, Z. Zhou, H. Liu, C. Wu, H. Zhang, G. Huang, H. Ai and J. Gao, *Nanoscale*, 2015, **7**, 6843–6850.

28 J. C. Park, G. T. Lee, H.-K. Kim, B. Sung, Y. Lee, M. Kim, Y. Chang and J. H. Seo, *ACS Appl. Mater. Interfaces*, 2018, **10**, 25080–25089.

29 J. Zhao, X. Li, X. Wang and X. Wang, *Nanoscale Res. Lett.*, 2019, **14**, 200.

30 L. P. Singh, N. V. Jadhav, S. Sharma, B. N. Pandey, S. K. Srivastava and R. S. Ningthoujam, *J. Mater. Chem. C*, 2015, **3**, 1965–1975.

31 T. Zhang, Z. Wang, H. Xiang, X. Xu, J. Zou and C. Lu, *ACS Appl. Mater. Interfaces*, 2021, **13**, 33850–33861.

32 L. S. da Costa, L. U. Khan, L. S. Franqui, F. de, S. Delite, D. Muraca, D. S. T. Martinez and M. Knobel, *J. Mater. Chem. B*, 2021, **9**, 428–439.

33 A. V. Lunin, I. L. Sokolov, I. V. Zelepukin, I. V. Zubarev, M. N. Yakovtseva, E. N. Mochalova, J. M. Rozenberg, M. P. Nikitin and E. L. Kolychev, *RSC Adv.*, 2020, **10**, 7301–7312.

34 A. de Espindola, C. S. Chagas, E. Barbosa, C. E. Castro, F. L. A. Fonseca, P. S. Haddad and C. Molina, *J. Magn. Magn. Mater.*, 2022, **545**, 168751.

35 A. I. Prasad, A. K. Parchur, R. R. Juluri, N. Jadhav, B. N. Pandey, R. S. Ningthoujam and R. K. Vatsa, *Dalton Trans.*, 2013, **42**, 4885.

36 C. Drivas, S. Kennou and G. Kyriakou, *Appl. Surf. Sci.*, 2025, **682**, 161672.

37 D. Prokopiou, M. Pissas, G. Fibbi, F. Margheri, B. Kalska-Szostko, G. Papanastasiou, M. Jansen, J. Wang, A. Laurenzana and E. Efthimiadou, *Toxicol. In Vitro*, 2021, **72**, 105094.

38 A. K. Gupta and M. Gupta, *Biomaterials*, 2005, **26**, 3995–4021.

39 J. Liu, C. Dai and Y. Hu, *Environ. Res.*, 2018, **161** 49–60.

40 K. D. Martinson, I. S. Kondrashkova and V. I. Popkov, *Russ. J. Appl. Chem.*, 2017, **90**, 1214–1218.

41 W. Chen, F. Li and J. Yu, *Mater. Lett.*, 2006, **60**, 57–62.

42 A. Mariani, M. Campetella, C. Fasolato, M. Daniele, F. Capitani, L. Bencivenni, P. Postorino, S. Lupi, R. Caminiti and L. Gontrani, *J. Mol. Liq.*, 2017, **226**, 2–8.

43 S. M. Masoudpanah, S. M. Mirkazemi, S. Shabani and P. T. Dolat Abadi, *Ceram. Int.*, 2015, **41**, 9642–9646.

44 M. Theodosiou, E. Sakellis, N. Boukos, V. Kusigerski, B. Kalska-Szostko and E. Efthimiadou, *Sci. Rep.*, 2022, **12**, 8697.

45 F. Margheri, C. Luciani, M. L. Taddei, E. Giannoni, A. Laurenzana, A. Biagioni, A. Chillà, P. Chiarugi, G. Fibbi and M. Del Rosso, *Oncotarget*, 2014, **5**, 1538–1553.

46 I. Y. Kim, T. G. Lee, V. Reipa and M. B. Heo, *Nanomaterials*, 2021, **11**, 1943.

47 Z. Darzynkiewicz, G. Juan and E. Bedner, *Curr. Protoc. Cell Biol.*, 1999, **1**, 8.4.1–8.4.18.

48 J. A. Pérez-Arizti, J. L. Ventura-Gallegos, R. E. Galván Juárez, M. del, P. Ramos-Godinez, Z. Colín-Val and R. López-Marure, *Chem. – Biol. Interact.*, 2020, **317**, 108966.

49 K. Bode, C. Link, P. Krammer and H. Weyd, *BIO-Protoc.*, 2020, **10**, e3737.

50 R. K. Shukla, A. Kumar, A. Pandey, S. S. Singh and A. Dhawan, *J. Biomed. Nanotechnol.*, 2011, **7**, 100–101.

51 E. Eruslanov and S. Kusmartsev, in *Advanced Protocols in Oxidative Stress II*, ed. D. Armstrong, Humana Press, Totowa, NJ, 2010, vol. 594, pp. 57–72.

52 M. Pedrino, P. Brassolatti, A. C. Maragno Fattori, J. Bianchi, J. M. de Almeida Rodolpho, K. F. de Godoy, M. Assis, E. Longo, K. Nogueira Zambone Pinto Rossi, C. Speglich and F. de Freitas Anibal, *Toxicol. Mech. Methods*, 2022, **32**, 213–223.

53 S. Elmore, *Toxicol. Pathol.*, 2007, **35**, 495–516.

54 M. Zimmermann and N. Meyer, in *Mammalian Cell Viability*, ed. M. J. Stoddart, Humana Press, Totowa, NJ, 2011, vol. 740, pp. 57–63.

55 I. Vermes, C. Haanen, H. Steffens-Nakken and C. Reutellingsperger, *J. Immunol. Methods*, 1995, **184**, 39–51.

56 D. Stephenson, T. Nemkov, S. M. Qadri, W. P. Sheffield and A. D'Alessandro, *Front. Physiol.*, 2022, **13**, 828087.

57 C. L. Williams, H. M. Neu, S. L. J. Michel and D. S. Merrell, Acinetobacter baumannii, in *Methods in Molecular Biology*, ed. I. Biswas and P. Rather, Springer New York, Humana Press, New York, NY, 2019, vol. 1946, pp. 195–205.

58 Y. P. He, Y. M. Miao, C. R. Li, S. Q. Wang, L. Cao, S. S. Xie, G. Z. Yang, B. S. Zou and C. Burda, *Phys. Rev. B*, 2005, **71**, 125411.

59 S. Bhattacharjee, *J. Controlled Release*, 2016, **235**, 337–351.

60 R. Xu, *Particuology*, 2008, **6**, 112–115.

61 M. Danaei, M. Dehghankhold, S. Ataei, F. Hasanzadeh Davarani, R. Javanmard, A. Dokhani, S. Khorasani and M. Mozafari, *Pharmaceutics*, 2018, **10**, 57.

62 A. S. Lawrie, A. Albanyan, R. A. Cardigan, I. J. Mackie and P. Harrison, *Vox Sang.*, 2009, **96**, 206–212.

63 D. Predoi, *Dig. J. Nanomater. Bios.*, 2007, **2**, 169–173.

64 M. Morel, F. Martínez and E. Mosquera, *J. Magn. Magn. Mater.*, 2013, **343**, 76–81.

65 Y. Wei, B. Han, X. Hu, Y. Lin, X. Wang and X. Deng, *Procedia Eng.*, 2012, **27**, 632–637.

66 G. B. Deacon and R. J. Phillips, *Coord. Chem. Rev.*, 1980, **33**, 227–250.

67 J.-G. Kang, Y. Jung, B.-K. Min and Y. Sohn, *Appl. Surf. Sci.*, 2014, **314**, 158–165.

68 I. L. Ardelean, L. B. N. Stoencea, D. Ficai, A. Ficai, R. Trusca, B. S. Vasile, G. Nechifor and E. Andronescu, *J. Nanomater.*, 2017, **2017**, 1–9.

69 K. Chinnaraj, A. Manikandan, P. Ramu, S. A. Antony and P. Neeraja, *J. Supercond. Nov. Magn.*, 2015, **28**, 179–190.

70 C. S. Ciobanu, E. Andronescu and D. Predoi, *Dig. J. Nanomater. Bios.*, 2011, **6**, 1239–1244.

71 R. Gabbasov, M. Polikarpov, V. Cherepanov, M. Chuev, I. Mischenko, A. Lomov, A. Wang and V. Panchenko, *J. Magn. Magn. Mater.*, 2015, **380**, 111–116.

72 V. G. Pol, O. Palchik, A. Gedanken and I. Felner, *J. Phys. Chem. B*, 2002, **106**, 9737–9743.

73 R. Marin and D. Jaque, *Chem. Rev.*, 2021, **121**, 1425–1462.

74 N. S. Leel, M. Kiran, M. K. Kumawat, P. A. Alvi, V. S. Vats, D. Patidar, B. Dalela, S. Kumar and S. Dalela, *J. Lumin.*, 2023, **263**, 119981.

75 A. V. Thorat, T. Ghoshal, P. Carolan, J. D. Holmes and M. A. Morris, *J. Phys. Chem. C*, 2014, **118**, 10700–10710.

76 D. F. Mullica, C. K. C. Lok, H. O. Perkins, G. A. Benesh and V. Young, *J. Electron Spectrosc. Relat. Phenom.*, 1995, **71**, 1–20.

77 N. S. Leel, S. Kumar, P. A. Alvi, B. Dalela, A. Sharma, S. Kumar and S. Dalela, *J. Magn. Magn. Mater.*, 2024, **603**, 172233.

78 A. Atrei, B. Lesiak-Orlowska and J. Tóth, *Appl. Surf. Sci.*, 2022, **602**, 154366.

79 X. Chen, X. Wang and D. Fang, *Fuller. Nanotub. Carbon Nanostruct.*, 2020, **28**, 1048–1058.

80 D. Briggs, *Handbook of X-ray Photoelectron Spectroscopy*, ed. C. D. Wagner, W. M. Riggs, L. E. Davis, J. F. Moulder and G. E. Muilenberg, Perkin-Elmer Corp., Physical Electronics Division, Eden Prairie, Minnesota, USA, 1981, vol. 3, v-v.

81 A. K. Friedman, W. Shi, Y. Losovyj, A. R. Siedle and L. A. Baker, *J. Electrochem. Soc.*, 2018, **165**, H733–H741.

82 K. Binnemans, *Coord. Chem. Rev.*, 2015, **295**, 1–45.

83 A. Ugale, T. N. Kalyani and S. J. Dhoble, *Lanthanide-Based Multifunctional Materials*, Elsevier, 2018, pp. 59–97.

84 S. Chaudhary, P. Sharma, S. Kumar, S. A. Alex, R. Kumar, S. K. Mehta, A. Mukherjee and A. Umar, *J. Mol. Liq.*, 2018, **269**, 783–795.

85 H. Terraschke and C. Wickleder, *Chem. Rev.*, 2015, **115**, 11352–11378.

86 C. D. Mungmode, D. H. Gahane and S. V. Moharil, Bikaner, India, 2018, p. 060037.

87 D. Kim, T. H. Kim, T. E. Hong, J.-S. Bae, C. H. Kim, J. Kim, S.-J. Kim, K.-W. Jeon and J.-C. Park, *Materials*, 2020, **13**, 1859.

88 L. Saravanan, R. Jayavel, S. S. Aldeyab, J. S. Zaidi, K. Ariga and A. Vinu, *J. Nanosci. Nanotechnol.*, 2011, **11**, 7783–7788.

89 Y.-F. Xu, D.-K. Ma, M.-L. Guan, X.-A. Chen, Q.-Q. Pan and S.-M. Huang, *J. Alloys Compd.*, 2010, **502**, 38–42.

90 E.-J. Cho and S.-J. Oh, *Phys. Rev. B: Condens. Matter Mater. Phys.*, 1999, **59**, R15613–R15616.

91 I. Choudhary, R. Shukla, A. Sharma and K. K. Raina, *J. Mater. Sci.: Mater. Electron.*, 2020, **31**, 20033–20042.

92 R. Meenakshi, V. T. Jisha and S. S. Soumya, *J. Sol-Gel Sci. Technol.*, 2024, **111**, 540–552.

93 M. V. Shestovskaya, A. L. Luss, O. A. Bezborodova, V. V. Makarov and A. A. Keskinov, *Pharmaceutics*, 2023, **15**, 2406.

94 N. Singh, G. J. S. Jenkins, R. Asadi and S. H. Doak, *Nano Rev.*, 2010, **1**, 5358.

95 O. A. Alabi, A. H. Silva, M. P. Rode, C. dal Pizzol, A. M. de Campos, F. B. Filippin-Monteiro, A. A. Bakare and T. B. Creczynski-Pasa, *Toxicol. Ind. Health*, 2021, **37**, 77–89.

96 T. Mai and J. Z. Hilt, *J. Nanoparticle Res.*, 2017, **19**, 253.

97 L. G. Rodriguez, X. Wu and J.-L. Guan, *Cell Migration*, Humana Press, New Jersey, 2004, vol. 294, pp. 023–030.

98 J. E. N. Jonkman, J. A. Cathcart, F. Xu, M. E. Bartolini, J. E. Amon, K. M. Stevens and P. Colarusso, *Cell Adhes. Migr.*, 2014, **8**, 440–451.

99 R. Meguro, Y. Asano, S. Odagiri, C. Li, H. Iwatsuki and K. Shoumura, *Arch. Histol. Cytol.*, 2007, **70**, 1–19.

100 M. Monici, *Biotechnology Annual Review*, Elsevier, 2005, vol. 11, pp. 227–256.

101 N. M. Cordina, N. Sayyadi, L. M. Parker, A. Everest-Dass, L. J. Brown and N. H. Packer, *Sci. Rep.*, 2018, **8**, 4521.

102 T. S. Blacker and M. R. Duchen, *Free Radicals Biol. Med.*, 2016, **100**, 53–65.

103 D. Gewirtz, *Biochem. Pharmacol.*, 1999, **57**, 727–741.

104 H. M. Al-Aamri, H. Ku, H. R. Irving, J. Tucci, T. Meehan-Andrews and C. Bradley, *BMC Cancer*, 2019, **19**, 179.

105 E. Lukášová, M. Řezáčová, A. Bačíková, L. Šebejová, J. Vávrová and S. Kozubek, *FEBS Open Bio*, 2019, **9**, 870–890.

106 Y.-P. Hsiao, H.-L. Huang, W.-W. Lai, J.-G. Chung and J.-H. Yang, *J. Dermatol. Sci.*, 2009, **54**, 175–184.

107 M. M. Al-Oqail, N. N. Farshori, E. S. Al-Sheddi, S. M. Al-Massarani, Q. Saquib, M. A. Siddiqui and A. A. Al-Khedhairy, *Oxid. Med. Cell. Longev.*, 2021, **2021**, 6695634.

108 S. Shukla, A. Jadaun, V. Arora, R. K. Sinha, N. Biyani and V. K. Jain, *Toxicol. Rep.*, 2015, **2**, 27–39.

109 U. S. Gaharwar, R. Meena and P. Rajamani, *J. Appl. Toxicol.*, 2017, **37**, 1232–1244.

110 M. Havrdova, K. Hola, J. Skopalik, K. Tomankova, M. Petr, K. Cepe, K. Polakova, J. Tucek, A. B. Bourlinos and R. Zboril, *Carbon*, 2016, **99**, 238–248.

111 C. Xue, J. Wu, F. Lan, W. Liu, X. Yang, F. Zeng and H. Xu, *J. Nanosci. Nanotechnol.*, 2010, **10**, 8500–8507.

112 S. Fu, S. Wang, X. Zhang, A. Qi, Z. Liu, X. Yu, C. Chen and L. Li, *Colloids Surf. B Biointerfaces*, 2017, **154**, 239–245.

113 Y. Liu, Y. Meng, Y. Zhu, L. Gu, A. Ma, R. Liu, D. Liu, S. Shen, S. Zhang, C. Xu, J. Zhang and J. Wang, *Regener. Biomater.*, 2024, **11**, rbae065.